The 2018-2019 seismo-volcanic crisis east of Mayotte, Comoros islands: seismicity and ground deformation markers of an exceptional submarine eruption

Anne Lemoine[1*], Pierre Briole[2], Didier Bertil[1], Agathe Roullé[1], Michael Foumelis[1], Isabelle Thinon[3], Daniel Raucoules[1], Marcello de Michele[1], Pierre Valty[4]

[1]BRGM, Direction Risque et Prévention, Orléans, France

[2]UMR 8538 CNRS - Ecole Normale Supérieure - PSL Research University, France

[3]BRGM, Direction Géoressources, Orléans, France

[4]IGN- Institut National de l'Information Géographique et Forestière / Service de Géodésie et Métrologie- St Mandé, France

a.lemoine@brgm.fr (*Corresponding author)

Key Points:

- In May 2018, an offshore seismic crisis began east of Mayotte, Comoros islands, including the largest event ever recorded in the Comoros. Earthquakes are clustered in space and time.
- The crisis was originally monitored with a sparse network of local accelerometers and regional broadband stations that was gradually completed.
- The volcanic nature of the crisis was originally supported by the displacement patterns of the permanent GNSS stations and InSAR observations on Mayotte, and by the occurrence of episodic very low frequency tremors, and later proven by direct observations at the sea floor.
- We present a model to interpret, at the first order, the combined spatiotemporal evolution of the seismological and geodetic data (GNSS and InSAR) during the first year of the crisis.
- The seismological and geodetic data allow us to discriminate and characterize the initial fracturing phase, the phase of magma intrusion from depth to the sub-surface, and the eruptive phase that starts in early July, fifty days after the first seismic events. The eruptive phase is still ongoing more than one year after initiation, but with an effusive rate that is half of the peak rate of late 2018.
- The inferred main deflation source is at a depth of 28 km, and the modelled extracted volume involved during the first year is around 2.3 km^3.
- This is the largest offshore volcanic event ever quantitatively documented.
- This is one of the largest basaltic eruptions of the last three centuries.

SUMMARY

On May 10th, 2018, a seismic crisis started ~50 km east of Mayotte, the easternmost of the Comoros volcanic islands. Over the course of one year, 32 earthquakes with magnitude greater than 5 occurred, the main one reaching $M_w = 5.9$ on May 15th, 2018.

This paper analyses the seismic crisis from the initiation through its first year. For this analysis, we confront the seismic spatio-temporal distribution with ground deformation observation (Global Navigation Satellite System, GNSS, and Interferometric Synthetic Aperture Radar, InSAR) and modelling.

The seismicity shows three successive clusters, migrating globally west to northwest (WNW) and overlapping in time and space. They are testimonies of fracturing and magma migration. During the first months of the crisis, the data of the GNSS stations and InSAR signals also evolve in three phases. At first, slight deformation was observed during two weeks at the beginning of the crisis, then deformation quiescence occurred from early June 2018 to early July 2018, and finally the main deformation phase started from early July 2018, which we interpret as the beginning of a large offshore eruption. It was followed by two months of seismic quiescence before renewal of seismicity at a lower level. One year later, the crisis is continuing with the persistence of an unusual seismicity, whose pattern has been similar since July 2018 (i.e., concentrated in two clusters), including episodic very low frequency tremors presenting a harmonic oscillation with a period of ~16 s and velocities measured by GNSS and InSAR that culminated during late 2018 and are smoothly decreasing since then.

A deflation model of a magma reservoir buried in a homogenous half space fits the data quite well. The introduction of a small secondary source allows for improvement of the fit by 30% and gives some first order information about how magma migrates beyond the deflation of the main chamber. From mid July 2018, the whole Mayotte island drifts at a slightly increasing rate until, in late 2018, reaching peak rates of ~224 mm yr^{-1} eastward and ~186 mm yr^{-1} downward. Since then, the deformation has smoothly decreased, reaching half of the peak rate in July 2019. The modelled deflating magma chamber is located 45 ± 5 km east of Mayotte, at a depth of 28 ± 3 km. The rate of magma extraction is ~94 $m^3 s^{-1}$ at the apex in late 2018 and ~44 $m^3 s^{-1}$ in July 2019. The total volume extracted from the deep source on July 2019 is 2.3 km^3.

INTRODUCTION

The volcanic Comoros archipelago (Fig. 1) is composed of four main islands, from west to east: Grande Comore, Mohéli, Anjouan, and Mayotte, and further east, the Geiser and Leven volcanic banks (Daniel et al. 1972). Volcanism in Comoros spans between the Miocene and Holocene. In Mayotte Island, the earliest phase of magmatic activity was dated 11 My ago (Debeuf, 2004; Pelleter et al., 2014), whereas the latest reported volcanic event occurred within a few thousand years in Petite Terre, East of Mayotte (Zinke et al., 2003). Due to relatively diffuse seismicity around Comoros archipelago associated with only a few historically felt events, Mayotte Island is usually associated with moderate seismicity.

The Mayotte volcano-seismic sequence began on May 10th, 2018. Over one year, we recorded 32 earthquakes with magnitudes greater than 5, the largest one reaching $M_w = 5.9$ on May 15th, 2018, the largest event ever recorded in Comoros. Such intense and long seismic activity has never been recorded before in the Comoros archipelago. More than one year after the onset of the crisis, the seismicity persists with a large number of small earthquakes (Bertil et al., 2019), episodic monochromatic Very Long Period (VLP) earthquakes, and the persistence of anomalous ground motion measured by Global Navigation Satellite System (GNSS) and Interferometric Synthetic Aperture Radar (InSAR) that followed ~2 months of intense seismic unrest at the beginning of the sequence.

There are several past examples of intense seismic activity associated with deformation in volcanic contexts, linked with magma migrations, intrusions, dike propagation, or eruptions. Regarding the intensity of the largest events, in Izu (Japan) in 2000 (Toda et al., 2002), five $M \geq 6$ events occurred within a few weeks. Seismicity and deformation patterns can be markers of magma intrusion especially through propagating and opening dykes, as in the Gulf of Aden, between November 2010 and March 2011 (Ahmed et al., 2016), where the spatio-temporal evolution of intense seismicity with 29 $M \geq 5$ earthquakes was interpreted as signs of magma ascent, followed by dyke propagations.

Seismo-volcanic crises can involve clustering, as in Afar (Ethiopia) where a phenomenon that began in 2005 involved seismicity organized in clusters, including $M > 5$ earthquakes. Then, between 2005 and 2010, 14 dike intrusions were identified along a 60 km long rift segment (e.g., Ayele et al., 2007; Grandin et al., 2011). Another example showing both seismicity and ground deformation patterns as markers of magmatic phenomenon is the rifting event near the Bárdarbunga volcanic system (Iceland) that lasted from August 16th to September 6th, 2014. As revealed by seismicity and ground deformation, it involved migrating seismic clusters, a 45 km long dyke intrusion magma source deflation and slow collapse of a caldera, magnitude $M > 5$ earthquakes, and effusive fissure eruption (Gudmundsson et al., 2014; Sigmundsson et al., 2015). Finally, the El Hierro eruption (Canary Islands) initiated on October 10th, 2011 and had been preceded since July 2011 by intense and fluctuant seismicity (including acceleration and migration, not exceeding $M_l = 4.3$) and by the concomitant evolution of deformation patterns. Pre-eruptive phases were distinguished, especially according to seismicity and displacement monitoring (López et al., 2012). Analysis of earthquake migration and surface deformation have shown that, after the initial fracturing and intrusion episode, a migration phase appeared and extended for ~20 km, preceding a submarine eruption (Martí et al., 2013).

The 2018-2019 seismo-volcanic activity is unusual due to its duration and the intensity of its seismic sequence and deformations, marking the end of a volcanic quiescence period in the Mayotte area.

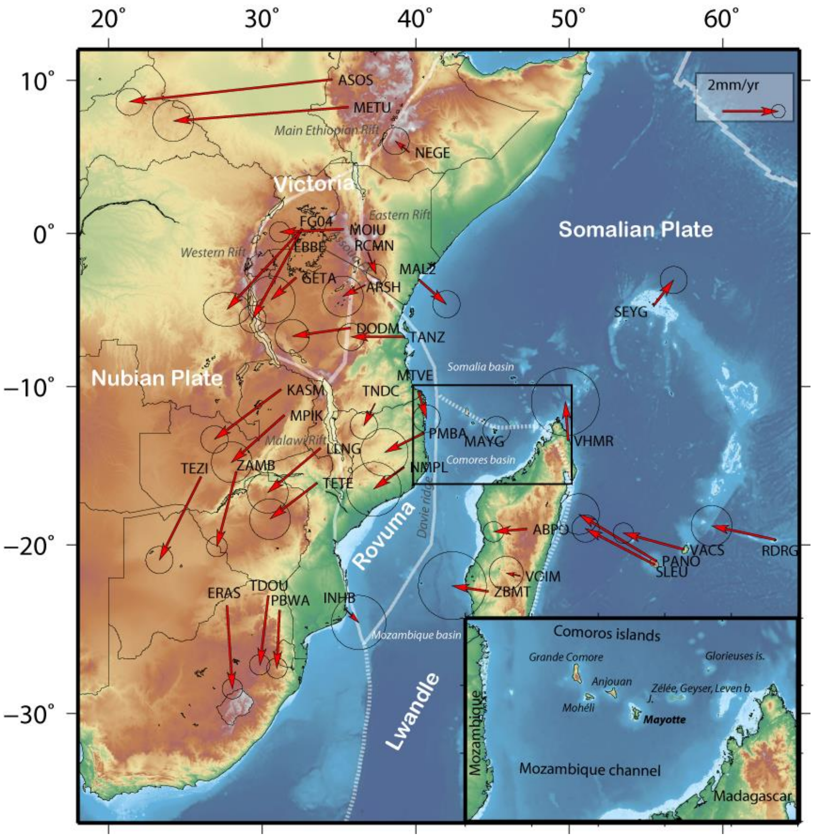

Figure 1. Velocity map for thirty-six GNSS stations around Mayotte (set to zero) from the time series published by the Nevada geodetic laboratory (Blewitt et al., 2018). The values are found in Appendix 1. A clockwise correction of 2.1° Myr^{-1} was applied to cancel the overall rotation around Mayotte. Main features in the area of the East African Rift are plotted (Davie Ridge, Eastern Rift, Main Ethiopian Rift, Western Rift, Malawi Rift, and Assoua Fracture Zone). The plate boundaries in white lines are modified from Saria et al. (2014) and Stamps et al. (2018). Elevation grid is from Gebco_2014 (Weatherall et *al.*, 2015). Inset: The Comoros islands surrounded by the Somali and Comoros basins. Bathymetry from Gebco_2014 completed around Mayotte by SHOM (2015) data. J. represents Les Jumelles: bathymetric edifices lying NE from Mayotte.

This seismo-volcanic crisis has been monitored since the beginning of the unrest with an evolving seismic network, originally not adapted to fine volcanic seismicity monitoring. From May 10th, 2018 to May 15th, 2019, the seismic monitoring network remained sparse, but allowed for the analysis of the evolution of the seismicity pattern. Permanent GNSS stations added to InSAR data registered different displacement patterns that we identified as different eruptive phases. Here we present an analysis of the first year of the Mayotte 2018-2019 seismo-volcanic episode combining both preliminary seismological analysis (including observation of atypical long-lasting very low frequency events) and deformation observations (GNSS and InSAR) before the significant improvement of the initial seismic monitoring network operated through the installation of ocean bottom seismometers (OBS) in May 2019. We propose a calendar of the events with scenarios that confronted the spatio-temporal evolution of seismological and geodetic observations to models that could explain different episodes of the seismo-volcanic phenomenon, including a model of a deflating magma chamber.

1 GEOLOGICAL SETTING AND REGIONAL CONTEXT

The Comoros Islands form an overall East-West (EW) trending archipelago located north of the Mozambique Channel, between the eastern coast of Mozambique and the northern tip of Madagascar (Fig 1). North of the Comoros Archipelago, most authors agree that the crust of the Somali basin is oceanic dating to the Mesozoic time (Ségoufin and Patriat, 1981; Rabinowitz et al., 1983; Malod et al., 1991; Sauter et al., 2018) from 152 Ma to 120 Ma (Davis et al., 2016). South to the archipelago, the nature of the Comoros basin is still debated between a thinned continental crust (e.g., Flower & Strong 1969; Bassias and Leclaire, 1990; Roach et al., 2017) and an oceanic crust setting during the Jurassic Magnetic Quiet Zone (Talwani, 1962; Recq et al., 1982; Rabinowitz et al., 1983; Klimke et al., 2016). The present-day morphology of this area arose from the Permian-Triassic Karro northwest-southeast (NW-SE) rifting, which resulted in the separation between Gondwana and Madagascar continental blocks (e.g., Malod et al., 1991; Davis et al., 2016). The Mozambique and Somalia basins opened while Madagascar Island drifted southward along the Davie ridge (Fig. 1). The tectonic regime in the Mozambique Channel is dominated by overall east-northeast by west-southwest (ENE-WSW) extension, which is also identified with the East African Rift System and Madagascar (e.g., Bertil & Regnoult, 1998; Piqué, 1999; Delvaux et al., 2010).

The Comoros archipelago began emplacement during the Cenozoic in the northern Mozambique Channel. Michon (2016) proposed that magmatic activity first appeared in Mayotte, ~20 Ma ago and then in Anjouan, Mohéli, and Grande Comore ~10 Ma ago. Comoros volcanism seems synchronous with volcanism in surrounding areas, i.e., in Madagascar and in some provinces linked to the East-African Rift System (e.g., Nouguier et al., 1986; Debeuf, 2004; Michon, 2016). According to rock geochronology (e.g., Nouguier et al., 1986; Debeuf, 2004; Pelleter et al., 2014), the youngest volcanic activity is in Grande Comore (0.13 ± 0.02 My to present) with the active Karthala volcano, and the oldest was reported in Mayotte (~11 My), with a similar age reported in Anjouan. In Mayotte, these authors identify different eruptive phases separated by quiescent periods. The northeast area of Mayotte is composed by a more recent volcanic complex dated from 500 ky to 150 ky in Grande-Terre and up to 4 ky in Petite-Terre (Nehlig et al., 2013; Pelleter et al., 2014). According to Zinke et al. (2003a, 2003b), the latest volcanic events documented are some ash deposits in the barrier reef between 4 and 7 ky. Offshore, on the insular slope of Mayotte, tens of small volcanic seamounts are observed in the north, northwest, and northeast parts (Audru et al., 2006) and is mainly distributed off Petite Terre along a WNW-ESE ridge where a new active volcanic structure has recently been documented (Feuillet et al., submitted).

Different debates are concerned with the cause of the Comoros volcanism: it could be linked to the presence of a hot spot, based on the westward migration of volcanism age (e.g., Emerick & Duncan 1982), or to the influence of lithospheric fractures (Nouguier et al., 1986). Recent work (Debeuf, 2004; Michon, 2016) suggests a mixed solution; regional extensive tectonics interacting with asthenospheric processes.

A catalogue of instrumental seismicity of the Comoros was extracted for 1964-2018 from the International Seismological Center (ISC, 2016) catalogue. For 1978-1995, it was completed using the Malagasy catalogue (Bertil & Regnoult, 1998), which lowers the detection threshold, depending on the distance from Tananarive (from mb ≈ 4.0 eastward from Mayotte to mb ≈ 4.3

around Grande Comore). The location accuracy is poor, up to 30 km for many events in this poorly instrumented region. The Mozambique Channel seismicity is marked by a north-south (N-S) band of activity (Fig. 2), associated with Davie Ridge (see Fig. 1) showing normal faulting mechanisms (Grimison and Chen, 1988). A zone of diffuse seismicity, ~100 km wide, runs E-W from 48°E and 42.5°E along the volcanic line of the Comoros islands (Fig. 2). From 1982 to 2016, eight moderate earthquakes occurred (M_w 5.0 to 5.3), spread throughout this band presenting normal faulting and strike-slip earthquakes, especially east of Mayotte (Fig. 2). In Madagascar, a moderate and distributed seismicity is associated with pre-existing structures and an overall E-W extension (Bertil and Regnoult, 1998; Rindraharisaona 2013).

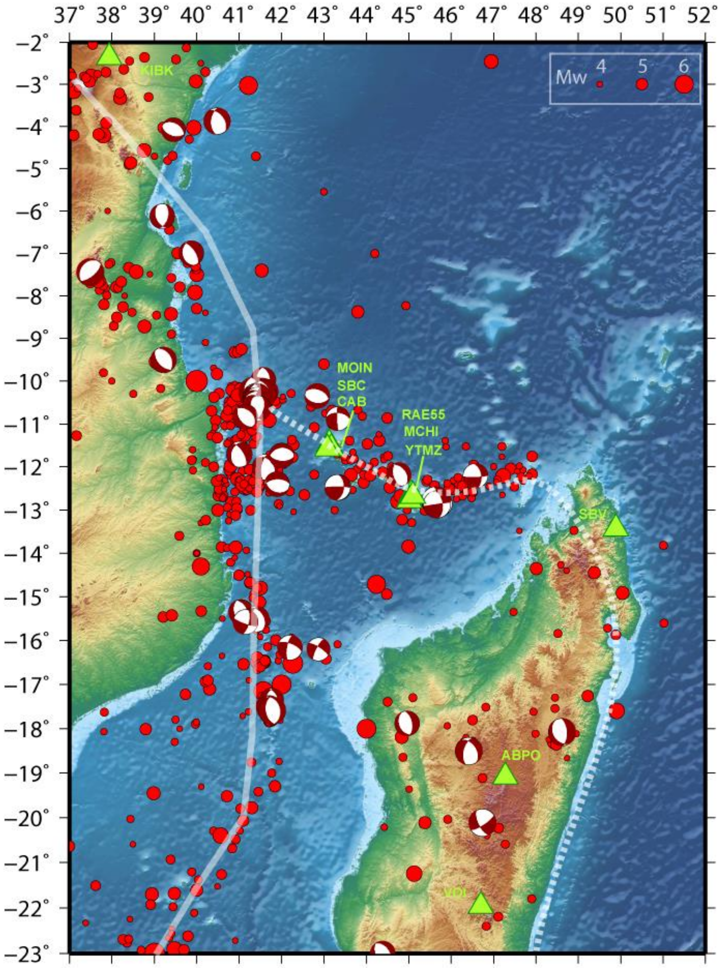

Figure 2. The 1901-2018 seismicity for M > 4 is created by merging the International seismological centre (ISC, 2016) catalogue and regional catalogue (Bertil & Regnoult, 1998; Bertil et *al*., 2018, 2019). The focal mechanisms for 1976-2019 are from the Global centroid moment tensor catalogue (G-CMT, Dziewonski et *al*., 1981; Ekström et *al*., 2012). The plate boundaries represented by white lines are modified from Saria et *al*. (2014) and Stamps et *al*. (2018). The bathymetry and topography are from Gebco_2014. Green triangles show the location of the seismic stations forming our monitoring network.

Several branches of the Cenozoic East African Rift System (EARS) form a distributed plate boundary zone between the Nubia and Somalia plates (e.g., Calais et al., 2006; Déprez et al., 2013; Delvaux & Barth, 2010; Stamps et al., 2018) where several authors (Hartnady, 2002; Horner-Johnson et al., 2007; Saria et al., 2014 or Stamps et al., 2018) defined three micro plates: the Victoria, Rovuma, and Lwandle blocks (Fig. 1). The boundaries of the Lwandle block are potentially diffuse and poorly constrained, especially with Somalia (Horner-Johnston et al., 2007; DeMets et al., 2010; Saria et al., 2014).

The overall actual trend of E-W extension over the East African region is illustrated by seismicity pattern (Fig. 2), geodetic observations, and the expression of extensive tectonics from EARS to Madagascar, including Mozambique Channel and Comoros volcanic axis (e.g., Bertil and Regnoult, 1998; Delvaux and Barth, 2010; Rindraharisaona et al., 2013; Stamps et al., 2018). Deville et al. (2018) reported extensional and trans-tensional fault systems, respectively, north and south of Mozambique Channel. Along the Comoros axis, the few available focal mechanisms show normal faulting and strike slip, compatible in terms of orientation to a NE-SW tensional axis.

The NE-SW extension across the line formed by the Comoros islands is also revealed by GNSS data. Fig. 1 shows velocities observed on available regional GNSS stations relative to Mayotte (MAYG station, Appendix 1). North of 19°S where the Davie Ridge is bending, both GNSS (Fig. 1) and focal mechanisms (Fig. 2) confirm the presence of a NE-SW tensional axis. The GNSS station distribution is uneven and particularly sparse around Comoros. Nevertheless, velocity at SEYG (Seychelles) is compatible with extension near the Comoros axis or in between them if the Somalia plate was undergoing small internal deformation. Moreover, velocities observed at PMBA and NMPL (Mozambique, Appendix 1) are also compatible with NE-SW extension that could be accommodated in Mozambique Channel, along Davie Ridge and the Comoros axis. The extension rate between PMBA and NMPL in Mozambique and SEYG in the Seychelles is of 2.6 ± 0.5 mm yr^{-1} with the azimuth N50°. Such an orientation is consistent with the focal mechanisms reported in Fig. 2 along the Comoros archipelago: normal faulting and strike-slip events, W and SSE of the Comoros that could indicate a trans-tensional stress regime. As, on one hand, the Comoros axis has been associated with volcanism since 20 Ma, and on the other hand, active seismicity is observed along this axis, whereas no identified seismicity is observed within the Somalia basin, between Seychelles and Comoros archipelago, we suppose that at least part of the NE-SW extension between Seychelles and Mozambique is accommodated across the volcanic line of the Comoros. Only few active structures are mapped on the seafloor around Comoros archipelago, and sparsely distributed GNSS and seismological stations add only a few reported focal mechanisms, leading to uncertainties in the description of the regional stress pattern.

Furthermore, VHMR and MTVE GNSS stations (Fig. 1), respectively, at the northern tip of Madagascar and in the Tanzania coastal area, point in opposite directions (relatively to Mayotte station MAYG), indicating rotating movement. South of the Davie ridge is dominated by left lateral shear at a rate of 1 mm yr^{-1}, according to the difference of velocities between PMBA and NMPL on the Rovuma plate and ABPO, VOIM, and ZMBT on the Lwandle plate (Fig. 1).

Of note, between the Neogene and Quaternary, tectonic and volcanic activities occurred in several branches in EARS (e.g., Déprez et al., 2013), but also in Madagascar (e.g., Rindraharisaona et al., 2013) and in Comoros (Nouguier et al., 1986; Debeuf, 2004; Michon, 2016). Michon (2016) proposed that the Comoros archipelago could potentially coincide with the eastern border of the EARS. Debeuf (2004) discussed the influence of extension linked to the East African Rift on Comoros volcanism. She mentioned the presence of an ancient regional lithospheric structure: the

Assoua fracture zone (east Africa), a Precambrian lineament of lithospheric dimension that, despite its age, could have localized the ascent of asthenospheric plumes in the recent geologic past.
In a poorly instrumented area where geological and geodynamical context are still not constrained, the Comoros archipelago (Mayotte island) is considered a moderate seismicity zone.

3. SEISMICITY OF MAYOTTE AND THE SEISMIC CRISIS OF 2018-2019

3.1 Historical seismicity

There are only a few testimonies of historical seismicity in the Comoros before the 20th century. Hachim (2004) identified some damaging earthquakes in Mayotte in 1606, 1679, and 1788 from oral transmission without being able to constrain testimonies from bibliographical data. Gevret (1870) and Vienne (1900) only quote felt earthquakes in Comoros Archipelago in 1808, 1829, and 1865, without any detail, and the 1829 event could have been misinterpreted; Lambert (1997) associated it with cyclonic phenomenon. From 1910 to 1960, the Malagasy academy published a catalogue of locally felt earthquakes made by the Tananarive observatory. More recently, regional felt earthquakes were reported in Sisfrance Océan Indien (2010). The January 16th, 1936 earthquake, west of Mayotte, was felt across the whole Comoros, causing moderate damage in several municipalities (La Dépêche de Madagascar, 19/02/1936, BNF). No historical chronicle documents any seismic cluster in Comoros.

3.2 Instrumental seismicity

Regarding the instrumental period, the catalogue of seismicity we built for the Comoros (see preceding chapter) contains some events within 150 km near the Mayotte edifice. Some events occurred south of Mayotte, including a mb = 5.0 event, on April 23rd, 1993, located ~40 km south of the island. East of Mayotte (~150 km), a patch of seismicity seems to be located around Zélée bank, including a magnitude 5.1 event on June 23rd, 2007 showing a strike-slip fault mechanism processed by the Global Centroid Moment Tensor (G-CMT, Dziewonski et al., 1981; Ekström et al. 2012). The last significant event close to Mayotte to occur before the 2018-2019 crisis was located forty km west of the island . It was a mb = 5.2 earthquake that occurred on 1 December, 1993 and was associated with moderate damage (Lambert, 1997). Close to this event, a normal faulting earthquake occurred on September 9th, 2011 (Mw = 5.0). No significant events were reported near the 2018-2019 seismic sequence during the instrumental period (in a poorly instrumented region associated with poor location accuracy and high detection threshold).

3.3 The 2018-2019 seismic sequence

The 2018-2019 seismic crisis is the first long lasting crisis reported in the instrumental catalogue of the Comoros or by testimony. When it started, the monitoring network consisted of four stations only: the accelerometer YTMZ from the French RAP (Réseau Accélérométrique Permanent) network (RESIF, 1995) in Mayotte, ~50 km west of the crisis (Fig. 3) and, at more than 650 km, the broad-band stations ABPO and VOI in Madagascar and KIBK in Kenya from IRIS/IDA seismic network (Incorporated Research Institution for Seismology/International Deployment of Accelerometers, Scripps Institution of Oceanography, 1986) and GEOFON seismic network (GEOFON Data Centre, 1993) global networks (Appendix 2). Late May, three broad-band stations (MOIN, SBC, and CAB) in Grande Comore, 280 km WNW of Mayotte (Fig. 2) hosted by the Khartala volcano observatory were integrated into the monitoring network thanks to the Institut de Physique du Globe de Paris (IPGP). On June 27th, three stations were added in Mayotte: a broadband station from Edusismo (MCHI) and two RaspberryShake stations (RAE55 and RCBF0) installed by the Bureau Central Sismologique Français (BCSF). Although not improving the coverage in azimuth or range, they contribute to lowering the detection threshold. Finally, on July 15th, the SBV GEOFON broadband station, northern Madagascar, 450 km east of Mayotte, resumed acquisition; it is a key station because it is the only one covering the seismic crisis from the east. With those eleven stations (Appendix 2, Fig. 2), the network is still not optimal with gaps in the azimuth and a lack of OBS close to the events. Nevertheless, it allows sharper detection than those from global networks such as the United States Geologic Survey earthquake catalog (USGS), with a detection threshold lowered around magnitude 3 instead of 4.5, and a catalogue completeness from magnitude 3.5, allowing the finest analysis of the temporal evolution of seismicity. However, during the most active period of the seismic sequence (especially from May 15th, 2018 to June 20th, 2018), catalogue completeness was higher, and we could not locate ml < 4.0 events. Due to network evolution through June 27th, detection thresholds have changed during the seismic sequence. The threshold is much higher for the initial period than for the following, though it was the more intense seismic phase.

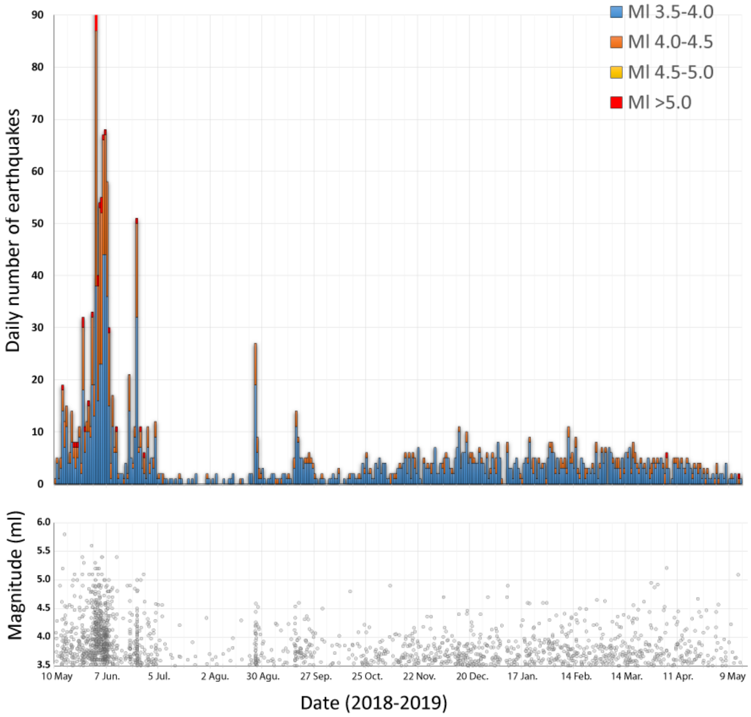

Figure 3. (top) Daily magnitude ranges of the 1748 $m_l>3.5$ events recorded from May 10th, 2018 to May 15th, 2019, modified from Bertil et al. (2019). (bottom) Magnitude distribution for $m_l > 3.5$ events.

In this paper, we present an analysis of seismicity from the beginning of the crisis until May 15th, 2019, when three broad-band seismic stations completed the sparse local monitoring network in the framework of the INSU Tellus SISMAYOTTE Program. In parallel, OBS were deployed at the end of February 2019 and retrieved May 2019, leading to a good azimuthal coverage of the seismic sequence that would permit the finest analysis of seismicity distribution (Feuillet et al., submitted).

From May 10th, 2018 to May 15th, 2019, we identified 1872 $m_l > 3.5$ events (Fig. 3). To those recorded at YMTZ, we assigned a local magnitude $m_l = 0.9 \log(pga) + 2.56 \log(d) - 0.16$, with pga (peak ground acceleration) in m s^{-2}, and d (hypocentral distance between YTMZ and the event) in km. This formula was constructed in order to minimize the scatter between m_l and the USGS m_b for the few tens of common events, occurring mostly in May and June, i.e., when largest events of the crisis were detected by international networks. Our local magnitude m_l is also aligned with the Seiscomp3 (Hanka et al., 2002) M_{lh} and M_{lv} for the largest events and for local stations on Mayotte. There are 27 events also processed by the (G-CMT with an average scatter between m_l and M_w of 0.2 (Appendix 3).

The crisis started on the morning of May 10th, 2018 with small events detected by the YTMZ accelerometer only. In the evening, a $m_l = 4.3$ event, not detected by the global networks, was the first event felt in Mayotte. From May 13th to 15th, the activity increased gradually with four events with m_l between 4.5 and 5 (Fig. 3 and 4). The main event, and largest ever recorded in the Comoros, with magnitude $m_l = 5.8$ and $M_w = 5.9$ (G-CMT), occurred on May 15th, 2018. Then the seismicity was relatively steady for the following ~15 days with 10 to 30 $m_l > 3.5$ events per day. Two strong events occurred on May 20th and 21st ($M_w = 5.5$). Between June 1st and 7th, the seismicity culminated with 52 to 87 $m_l \geq 3.5$ events daily, with the highest activity on June 1st, 2018. After June 7th, 2018, the seismicity decreased. It increased again between June 19th and 27th, 2018 with several $m_l \geq 5.0$ events with a new peak of activity on June 23rd, 2018 (50 $m_l \geq 3.5$ events). The period between July 10th and August 26th is quiescent with a sharp drop in the number and magnitude of events (Fig. 3). On August 26th, eight events between $m_l = 4$ to 4.5 occurred (27 $m_l \geq 3.5$ events), initiating a renewal of activity with two $m_l = 4.8$ events occurring on October 16th and November 7th, marking the last day associated with such a high level of activity (afterward, the maximal daily number of $m_l \geq 3.5$ events were 14). However, their contribution to the total moment release is low compared to the first weeks of activity (Fig. 4). Since October 2018, a relatively steady level of active seismicity is observed that began to lower at the end of April 2019 (Fig. 3 and 4).

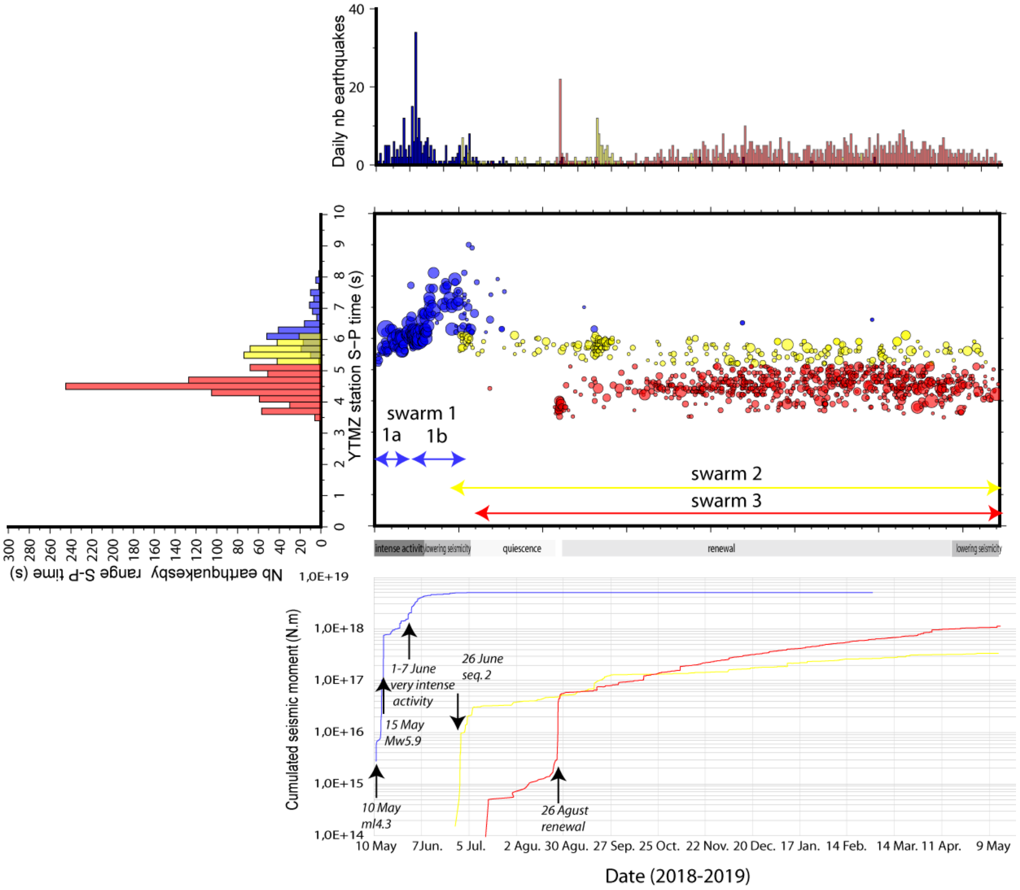

Figure 4. (left) S-P time distribution at YTMZ station by cluster (blue for cluster 1, yellow for cluster 2, and red for cluster 3). (top right) Daily number of ml≥3.5 events for each cluster. (middle right) Evolution of S-P time from YTMZ station with time. Three clusters are identified. Cluster 1 (blue) is mainly active from May 10th, 2018 to early July 2018. Cluster 2 (yellow) starts on June 26th, 2018 and remains active until the end of the observation period. Cluster 3 (red) begins in July 2018 and is also still active on May 15th, 2019. (bottom right) Cumulative seismic moment for the three clusters.

For the seismic moment, we use the equation $Mo = 10^k$, with $k = 1.5\ m_l + 9.1$ (Aki & Richards, 2002) that we compared to the available G-CMT values. The cumulated seismic moment for the whole period corresponds to a $M_w = 6.5$ event, with most of the seismic moment released before early July 2018. The most active period, from June 1st to June 7th, 2018, corresponds to a $M_w = 6.2$ event, more than the $M_w = 5.9$ of the largest event from May 15, whereas the largest magnitude registered in this period is $m_l = 5.3$. In comparison, the cumulative seismic moment from 1977 to 2017 for the entire Comoros (between 42.5° E and 48° E) represents less than $M_w = 6.0$. Between August 1st, 2018 and May 15th, 2019, the cumulative seismic moment released corresponds to a $M_w = 6.1$ event. After a quiescent phase from July 13th to August 26th, 2018, there is a resurgence of seismic activity at the end of August with lower intensity and low contribution to the moment release (Fig. 3, Fig. 4).

Only 1163 of the 1872 $m_l \geq 3.5$ events could be localized using crustal phases for distances ≤ 1200 km, 32 of them corresponding to $m_l \geq 5$ and 161 to $m_l \geq 4.5$ (Fig. 5). The magnitude threshold for locating the events was a function of both the network geometry and the intensity of the seismic activity. From May 10th to May 30th, 2018, all events with $m_l \geq 4.5$ were localized, but not all those with m_l between 4 and 4.5. During the intensive period between May 30th and June 7th, we could not localize some events with m_l around 4.5 due to the sparse network and too many repeating events leading to mixing seismic phases. From June 7th to June 27th, 2018, all $m_l \geq 4$ were localized. After June 27th, 2018, the catalogue of localized events is complete for all $m_l \geq 3.5$ and the magnitude catalogue is complete from $m_l \sim 3.5$, thanks to a phase of network improvement. We used the Seiscomp3 location algorithm LOCSAT (Nagy, 1996) and the standard one-dimensional (1D) velocity model IASP91 from Kennett (1991), as there is no velocity model available for the region, but we modified the Vs Table corresponding to a Vp/Vs ~ 1.72 for distances lower than 1200 km. We arbitrary fixed all events at 10 km depth in this context of sparse instrumental coverage where neither local velocity models nor lithospheric structure are known. Our horizontal accuracy is around 15 km (between 10 and 20 km, depending on the number of phases that can be used for locating), with longitudes better constrained than latitudes due to the network geometry. Hypocentral distance is a better reference in such a context, but still depends on an unknown velocity model. We choose to keep S-P time at YTMZ as a reference, as it is the only parameter common to the entire seismic sequence that is independent to location uncertainties or network evolution.

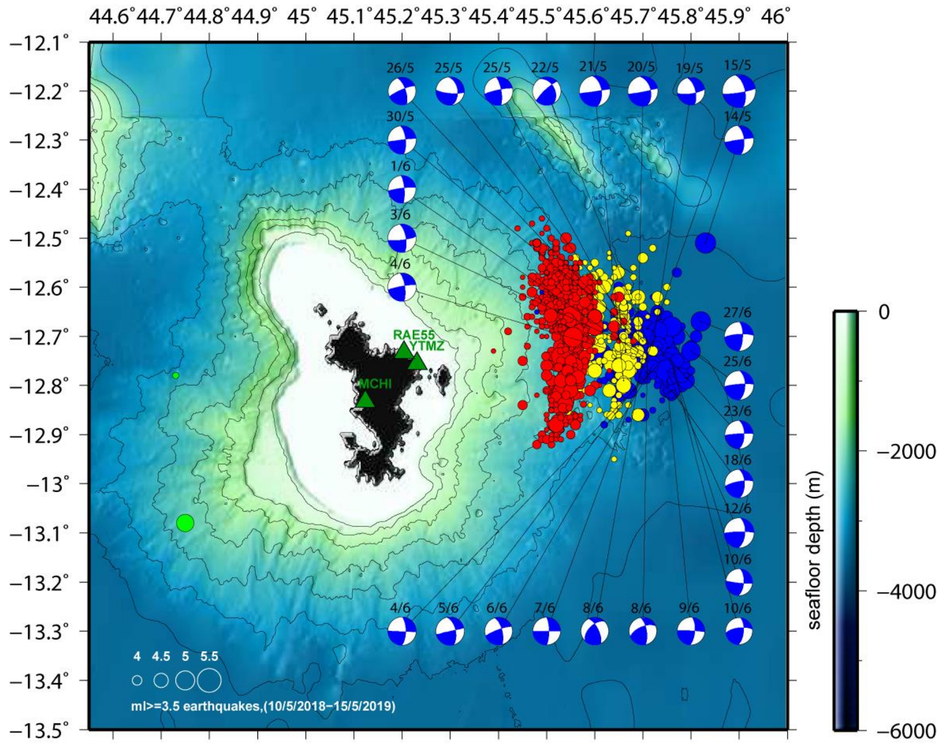

Figure 5. Localized earthquake map with $m_l \geq 3.5$ from May 10th, 2018 to May 15th, 2019. The first cluster (blue) is active mainly from May 10th, 2018 to early July 2018, the second (yellow) from June 26th, 2018, and the third (red) from mid July 2018. Green points represent earthquakes registered during the observation period but out of the clustering seismicity. The G-CMT focal mechanisms correspond to $m_l > 4.7$ events, all occurring from May 14th to June 27th, 2018. The bathymetry is from the Homonim project (SHOM, 2015) and Gebco, 2014 (Weatherall et *al*., 2015).

The seismicity is organized in three clusters, coherent in space and time (Fig. 4, Fig. 5). In the first one, active mainly from May 10th to beginning of July 2018, the events (blue dots) occurred in a ~20 km diameter area, corresponding to S-P time at YTMZ from 5.2 to 8.1 seconds (i.e. east of YTMZ, ~45 to 65 km considering hypocentral distance). This first cluster gathers all the largest events of the crisis, and shows a gradual increase of S-P time at YTMZ, especially from the beginning of June 2018 (Fig. 4), associated with a migration SE, with a total of ~10 km shift for the period (Fig. 6). SE migration is confirmed by G-CMT locations for the largest events (Fig. 7) associated in parallel with a depth change from 35 km to 15 km from early June 2018 (depth from G-CMT catalogue is decreasing from June 4th, Fig. 7), which is beyond the error bars and proof of upward migration. We distinguished two phases in this first cluster: cluster 1a from May 10th to the beginning of June 2018, and cluster 1b covering early June to beginning of July 2018, that started at the beginning of the seismically very intense first week of June. Cluster 1b is associated with the increase and spreading of S-P time reported at YTMZ and preceded its lowering at initial values at the end of June 2018. From the end of June 2018 (around June 26th) to July 2018, S-P time retrieves lower values equivalent to the beginning of the first cluster (between 5.2 and 6.1 seconds); the second cluster (yellow dots) starts westward from the latest events of the first cluster (Fig. 5), i.e., closer to YTMZ (hypocentral distance to YTMZ: ~42- 55 km). This second cluster could be potentially close to the initial position of the first cluster, before its migration (i.e., corresponding to cluster 1a). The two clusters overlap in time until the first one almost ends around July 8th, 2018. In July 2018, a third cluster starts (red dots), with S-P time at YTMZ from 3.3 to 5.1 seconds (i.e., corresponding to hypocentral distance to YTMZ of ~26 to 42 km), overlapping in time with cluster 2, but more energetic (Fig. 4 and Fig. 5). There is no evidence of epicentral migration in clusters 2 and 3, except at the beginning of cluster 2 with some more westward events. As a whole, the three clusters depict activity migrating WNW (Fig. 5) during the onset of the crisis until July 2018 (whereas inside the first cluster, a SE migration is observed, confirmed by G-CMT locations for the largest events), and then a steady seismicity pattern is observed.

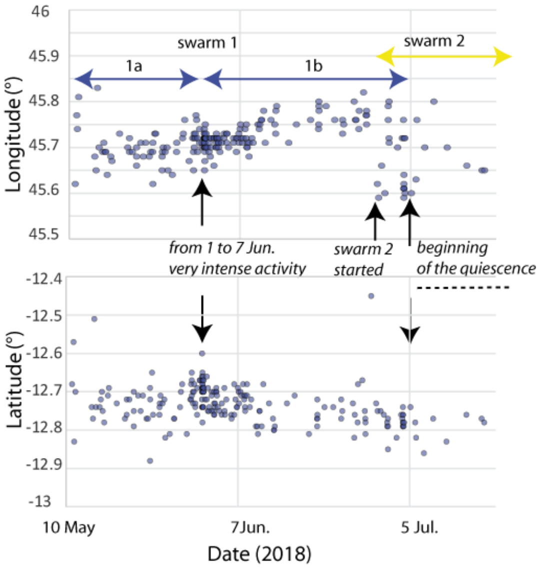

Figure 6. Eastward and southward migration of the seismicity within cluster 1 (ml≥3.5 events) that preceded the second cluster initiation and July-August 2018 seismic quiescence.

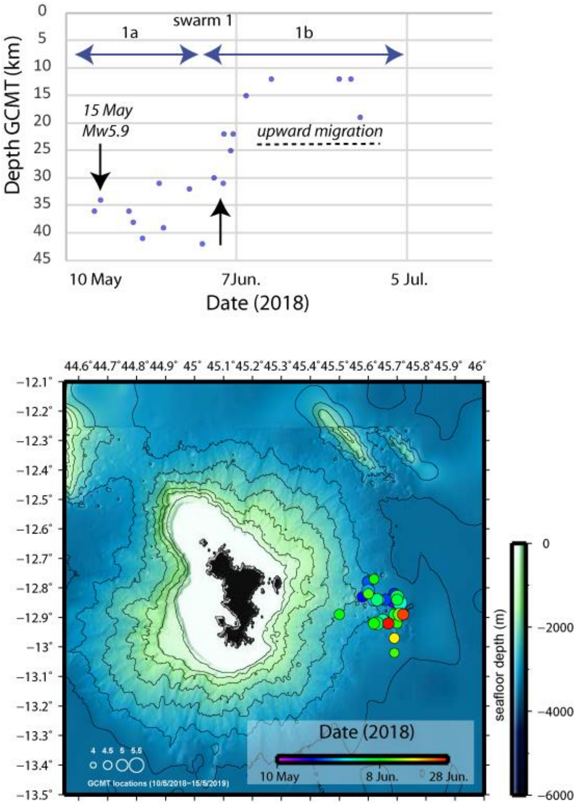

Figure 7. (top) Depth distribution of the seismicity as revealed by the depths determined by G-CMT for 19 events with $M_w \geq 4.9$, listed in Appendix 3. Upward migration is observed from early June 2018. (bottom) Twenty-seven G-CMT locations corresponding to the first cluster ($4.7 \geq M_w \geq 5.9$). As colours depend on date, SE migration appears in parallel to the upward migration.

Westward from the Mayotte edifice, two $m_l > 3.5$ earthquakes are reported in Fig. 5 (green circles): on May 13rd, 2018 ($m_l = 4.9$ located thanks to only 5 phases) and April 6th, 2019 ($m_l = 3.7$, with 12 phases). They occurred close to the epicentres of both the December 1st, 1993 damaging earthquake (Lambert, 1997, m_b 5.2) and September 9th, 2011 (M_w5, normal faulting, G-CMT) event. Intensive activity due to the 2018-2019 seismo-volcanic crisis may have induced changes in the stress pattern of the regional active structures.

We made a *b*-value analysis for the events with ml ≥ 3.5 by applying the Weichert method (Weichert, 1980) with magnitude steps of 0.1 (Fig. 8). The *b*-value is 1.2 for the whole period and 1.1 for cluster 1, close to classical *b*-values for tectonic areas (e.g., McNutt, 2005). The *b*-values for clusters 2 and 3 are 1.3 and 1.5; thus, higher and consistent with *b*-value anomalies observed at some volcanoes (e.g., *b*-value for Ito-Oki volcano is 1.5; Wyss et al., 1997).

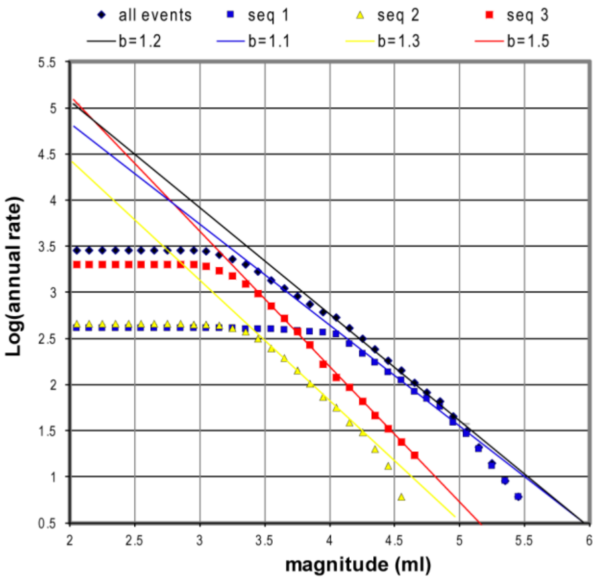

Figure 8. *b*-values for the three clusters and the whole sequence

The G-CMT fault planes are very similar for all events with averages and mean scatters of 352 ± 9°, 63 ± 9°, and 5 ± 13° for plane 1 and 260 ± 12°, 85 ± 11°, and 152 ± 9° for plane 2 (Fig. 5). Both indicate strike slip on a steep fault. The corresponding tension axis is oriented N34 ± 15°, which corresponds to a most favoured faulting azimuth N304°.

The 32 largest events ($m_l \geq 5.0$) are listed in Appendix 3 with their G-CMT moment when it exists. All together they correspond to 45 % of the total moment release from May 10th, 2018 to May 15th, 2019. All occurred during the first part of the seismic sequence, between May 14th and June 27th, 2018, except three events (March 28th, 2019, $m_l = 5.0$; April 5th, 2019, $m_l = 5.2$; and May 14th, 2019, $m_l = 5.1$). Most of them have similar strike slip focal mechanisms, indicating either right lateral shear along ~E-W structures or left lateral shear along ~N-S structures (Fig. 5). The former is more consistent with the relative movements of the plates from either side of the archipelago, i.e., counter-clockwise rotation of the Lwandle plate with respect to the Somalia plate (Saria et al., 2014), but the active structures that could be responsible for those mechanisms are still not identified. N-S structures would have the same orientation as ancient transform faults linked to ancient spreading in the Somali basin along the N-S direction (e.g., Rabinowitz et al., 1983). There are other strike-slip focal mechanisms around Comoros that have occurred since 1976 in the G-CMT catalogue (Fig. 2), making the whole consistent with a present-day ~NE-SW regional extensional or trans-tensional regime in the area.

4. VERY LOW FREQUENCY MONOCHROMATIC SEISMIC EVENTS

Several long lasting monochromatic very low frequency events (e.g., Tab. 1) have been recorded. They present decaying harmonic oscillations following a short onset, typical from Long-Period (LP) waveform patterns observed, for example, at Kusatsu-Shirane or Galeras volcanoes (Kumagai and Chouet, 1999), or described as “tornillos” by Gómez and Torres (1997), but they presented higher frequency oscillations and long lasting signals. The largest one, on November 11th, 2018, recorded worldwide, awoke the interest of the seismological community and the media (Fig. 9).

None of those long lasting monochromatic Very Low Frequency events, are triggered by a strong earthquake, but there are earthquakes embedded in all events observed, and all start with moderate and high frequency events (e.g., Fig. 10). Those signals are associated with elliptical particle motion and can be attributed to long monochromatic very low frequency Rayleigh waves (as shown in Fig. 11; e.g., elliptical particle motion in the vertical plane).

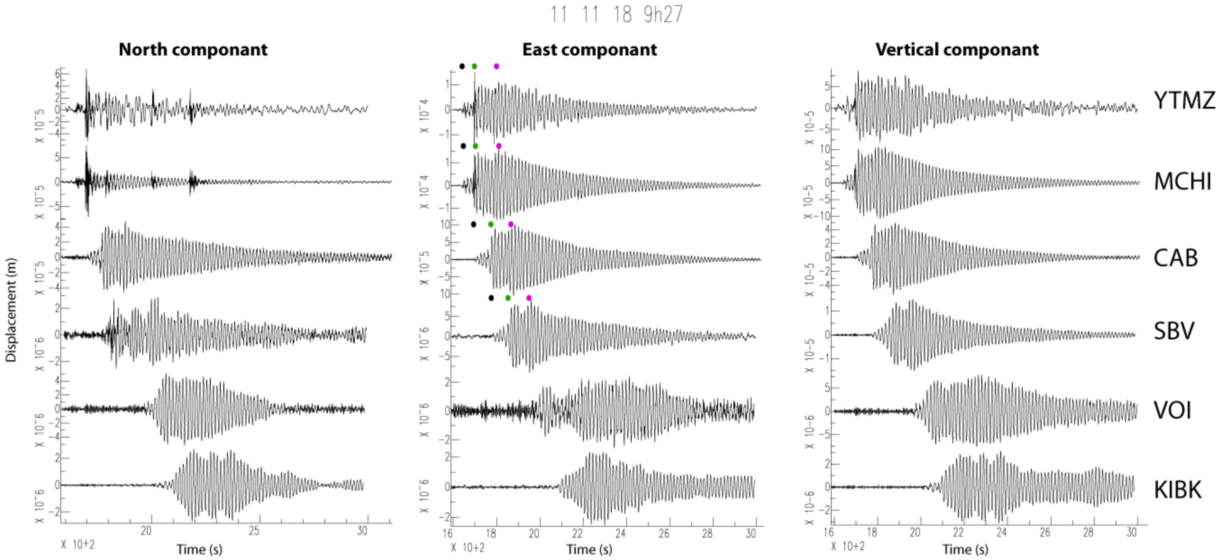

Figure 9. Displacement of local and regional stations, in meters, for the November 11th, 2018 very low frequency event. Black dots represent the initial excitation, green and purple dots are end and the beginning of the two embedded monochromatic damping phases.

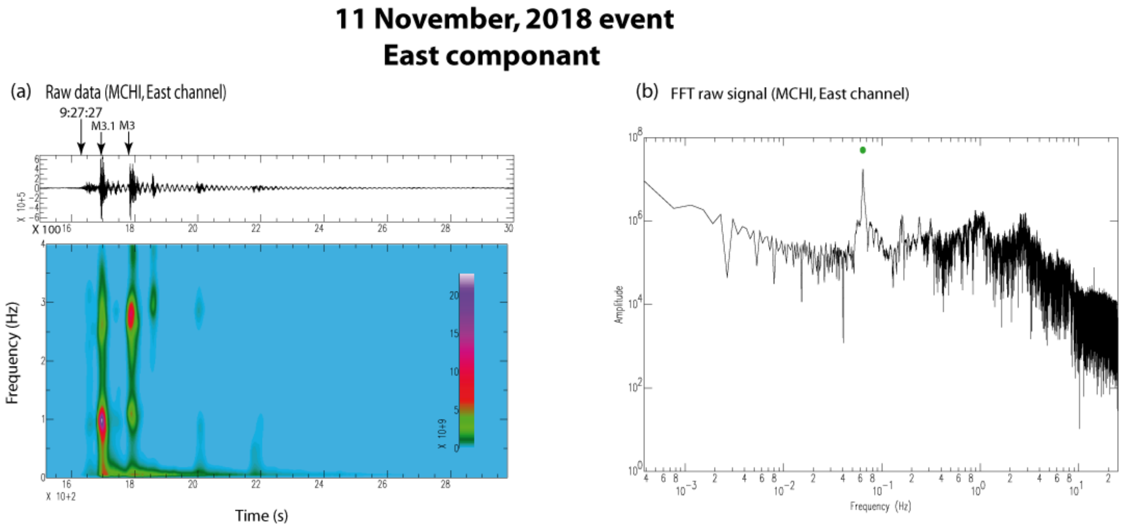

Figure 10. The November 11th, 2018 very low frequency tremor: (a) seismogram and spectrogram for the raw EW component of MCHI, (b) Fourier spectrum of the EW component of MCHI (peak at 0.062 Hz).

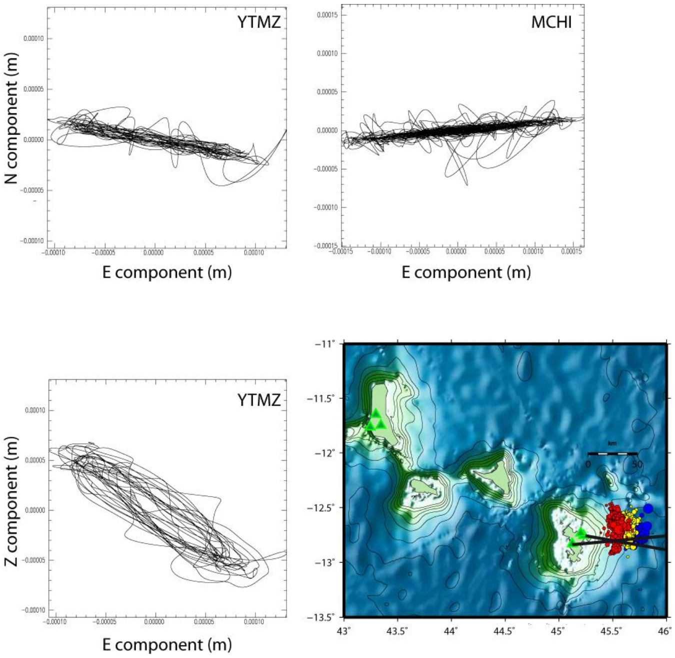

Figure 11. The November 11th, 2018 very low frequency event: particle motions at YTMZ and MCHI local stations and map showing the azimuth of the horizontal oscillation (black lines).

For the largest very low frequency event of November 11th, 2018, a small high frequency event occurs at 9:27:27 UTC, followed by small classical earthquakes, and then by the very low frequency monochromatic event that lasts more than twenty minutes, as shown by the E-W raw record of the local MCHI seismometer (Fig. 10a). Two earthquakes of $m_l = 3.1$ at 9:27:56 and $m_l = 3$ at 9:29:30 appear from the initial part of the signal. They are located at 45.49°E, 12.61°S and 45.47°E, 12.58°S, with a fixed depth of 10 km, within cluster 3. A third, smaller event occurs at 9:30:50, followed by two very small ones that we could not localize, but are well visible in the raw trace shown in Fig. 10. The spectrogram allows us to separate the long very low frequency signal from the higher frequency shorter events. The Fourier spectrum (Fig. 10b) shows a peak at ~0.062 Hz, thus a period of ~16 s corresponds to the very low frequency event integrated in the signal (green dot).

Fig. 9 shows the three displacement components for the November 11th, 2018 event at seven local and regional stations (mapped on Fig. 2 and Fig. 5), including the YTMZ accelerometer and velocimeters corrected by instrumental responses. After integration, the signal was filtered with a band of 0.05 to 1 Hz. In the case of YTMZ, there was a first integration with filtering between 0.01 and 10 Hz. Three distinct phases can be distinguished in the records. At the event onset, the first low frequency phase starts almost at the same time as the small high frequency signal that initiates the sequence (black dots, especially that of MCHI, on Fig. 9). For the local stations, this initial phase lasts around 1 minute. The second phase is the one with the oscillations and highest amplitude monochromatic waves (green dots). In the decay part of the harmonic oscillations, there are two embedded decay envelopes starting at the green and purple dots and lasting ~20-30 min. The duration of the monochromatic low frequency wave train seems not to depend on distance from the source. This characteristic was observed twice in 2011 and 2013, close to Rocard submarine volcano, Polynesia (Talandier et al., 2016). These two events share similarities with the

November 11th, 2018 event generated offshore Mayotte: both 2011 and 2013 intense Rayleigh wave trains were monochromatic (period observed was 17.0 s) and long-lasting (50-60 min in 2011 and 30-40 min in 2013).

Long period seismicity is considered to be related to magmatic and hydrothermal processes in a volcanic context, their signal can be linked to oscillations within an excited fluid-filled oscillator (e.g., Chouet, 2003). Physical properties of the resonator can be deduced from the signal characteristics. We modelled the decay envelopes of the very low frequency tremor from November 11th, 2018 (Fig. 12) with a model of a damped oscillator following the equation exp $(-t / \tau)$ with $\tau = 360$ s. From the physics perspective, this is compatible with the excitation followed by the free damping of a viscous fluid oscillating within a reservoir.

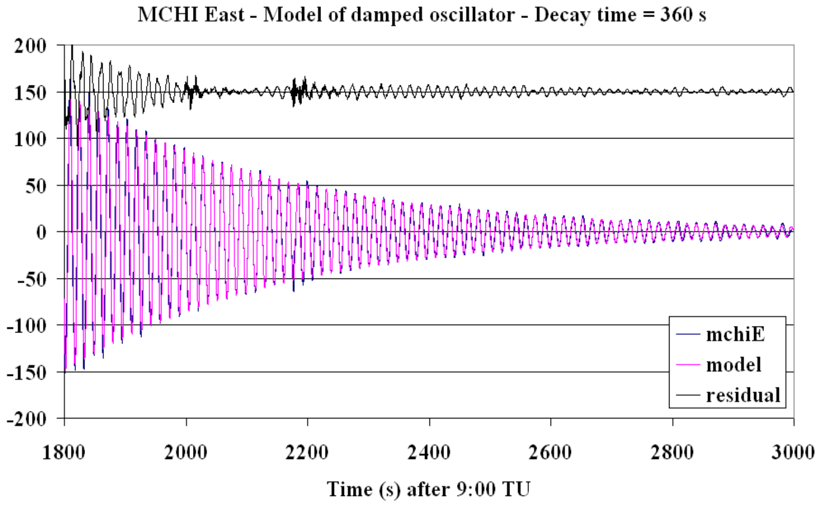

Figure 12. Modelling of the tremor decay for the east component of MCHI station. A model of a damped oscillator with decay time of 360 s fits the data (pink and blue lines which are almost superimposed) well and permits us to extract small earthquakes that occur during the tremor on the residual (in black).

Fig. 9 and Fig. 11 show that, especially at local stations YTMZ and MCHI, the low frequency tremor affects mainly the vertical and E-W components, and much less the N-S component, as indicated by particle motion. The particle motion calculated for YTMZ and MCHI shows how the oscillation is polarized during the monochromatic decay phase. Horizontal polarizations of the closest stations are used in order to estimate the position of the source: in Fig. 10, the black lines from YTMZ and MCHI on the map are converging towards the location of cluster 3, with the azimuth ~N85° from MCHI and ~N100° from YTMZ. An origin of this long lasting very low frequency tremor in the vicinity of cluster 3 would be coherent with the location of the small high frequency events observed at the onset of the signal. They could have represented the initial excitation, initiating oscillation of a resonator.

In an active volcanic context, high frequency earthquakes are commonly attributed to shear fracture due to magma migration (e.g., Toda et al., 2002; Battaglia et al., 2005; López et al., 2012; Martí et al., 2013; Gudmundsson et al., 2014; Sigmundsson et al., 2015). Detection of low frequency volcanic earthquakes in a volcanic area suggests that magmatic processes are active and can reveal different processes linked to magmatic or hydrothermal fluid processes (e.g., Chouet, 2003;

McNutt, 2005; Shapiro et al., 2017). Among them, some earthquakes are described by decaying harmonic oscillations after a short onset in the period range 0.2 to 2 s, characterized by one or more frequency peaks related to a source effect (e.g., Chouet, 1996; Chouet and Matoza, 2013). This pattern is interpreted as a time-localized pressure excitation mechanism followed by resonance of a fluid-filled cavity in response to the excitation. Damped oscillations can be described by its dominant frequency and quality factor that depend on the source properties: fluid types and resonator geometry (e.g., Kumagai and Chouet, 2000). Gómez and Torres (1997) reported such "tornillos" events in andesitic volcanoes just before or after eruptions, as well as during seismic swarms or quiescent periods. Characteristic frequencies seem to be different from one volcano to another. Signatures of signals recorded at Kusatsu-Shirane or Galeras volcanoes present a typical signature of long harmonic codas following a brief onset (Kumagai and Chouet, 1999) that exhibit similarities with the Mayotte November 11th, 2018 event, but with a lower range for the characteristic period and duration.

VLP events present longer periods, ranging between 2 and 100 s. They have been widely observed at numerous active volcanoes (e.g., reviews in MacNutt, 2005 or Chouet and Matoza, 2013). Among them, VLP signals observed at Hachijo volcano in 2002 present a decaying harmonic oscillation lasting 300 s with period ~10 s, a pattern that is similar to features of Long Period (LP) events with shorter period ~1 s. These VLP signals at Hachijo volcano were interpreted as the resonance of a basaltic magma in a dike (Kumagai et al., 2003). Kumagai (2006) proposed that the variation of frequency and quality factor of the harmonic oscillation are due to the gradual expansion of a crack containing basalt mixed with gas. Kawakatsu et al. (2000) reported that Long Period Tremors (LPT) with a dominant period around 15 s were observed at Aso volcano (Japan), with a short duration (less than one minute), both during periods of volcanic quiescence and unrest (Kawakatsu et al., 2000). These LPT are interpreted as a response of resonating fluid-filled cracks to pressurization within the hydrothermal system at Aso volcano (e.g., Hendrigana et al., 2019).

Long lasting VLF events observed by Talandier et al. (2016) in Polynesia, close to the submarine volcano Rocard (Society hot spot), are of volcanic origin, but different from usual volcano-seismic events recorded in areas that are associated with eruptive phenomena (e.g., high frequency harmonic tremor). Whereas seismicity related to an eruption is mainly a signature of magma transfer, Talandier et al. (2016) interpreted the Rayleigh monochromatic low frequency wave train as due to the strong hydrostatic pressure undergone by the volcanic edifice at 3200 to 4000 m depth below the sea surface. Under high hydrostatic pressure, magma movement can generate the resonance of a shallow opened conduit.

The November 11th, 2018 signal emitted offshore Mayotte is associated with a frequency peak included in the range of VLP seismology, but its waveforms are typical of some long period events ("tornillos" events) attributed to the decaying oscillation in a resonator. This event can be considered as an end-member of sources linked to resonator oscillation after excitation, similar to the two events reported in 2011 and 2013 in Polynesia (Talandier et al., 2016). Moreover, as several long-lasting monochromatic events presenting similar characteristics as the November 11**th**, 2018 event were observed (listed in Tab. 1), it should imply a non-destructive source process.

5. GROUND DEFORMATIONS

5.1 GNSS data

Six GNSS stations (Tab. 2) were operating in Mayotte at the beginning of the crisis, MAYG installed in 2014, all the others installed in early 2018. Their data are all gathered and routinely processed by the French IGN throught the public service RGP (Réseau GNSS permanent, http://rgp.ign.fr).

We used the four stations, BDRL, MAYG, KAWE, and GAMO, whose data are calculated by various processing centres, including the Nevada Geodetic Laboratory (http://geodesy.unr.edu) added by two other permanent GNSS stations (MTSA and PORO, Table 2). This allows us to compare solutions from various sources and, in particular, estimate a yearly periodic term at station MAYG. It is the only station where this component can be estimated because of the available four years of pre-crisis data. Although small, this component is important for taking into account the proper unbiased evaluation of the deformation over short periods of time. Fig. 13 shows the time series at station MAYG. The yearly term is assumed to have the form A sin (2π (t-to)/T) with A as amplitude, T = 1 year, and to as time origin. The best fitting values for the time origin to are August 8th, October 13th, and November 11th, respectively, for the east, north, and vertical components, with uncertainties of ~15 days, and amplitudes of 0.6, 0.9, and 2.6 mm, respectively. The horizontal amplitudes are not very large and not critical for our analysis because the deformation is much larger on these components. It is important to take the vertical term into account for evaluating, not the overall displacement (that is large), but its temporal variation. Due to the lack of data, the yearly components at the other stations could not be processed, so we use the values of MAYG for all stations. It has been observed in several other cases that the yearly effects are, in general, in phase at stations located in such a small area, though not necessarily with the same amplitudes (e.g. La Réunion island GNSS stations on http://rgp.ign.fr/). Therefore, the weaker point for us here is not the phase, but the assumption that the amplitude of the vertical yearly component is the same at all stations. This cannot be further assessed with the available data and a few more years of observation will be needed to estimate this more accurately.

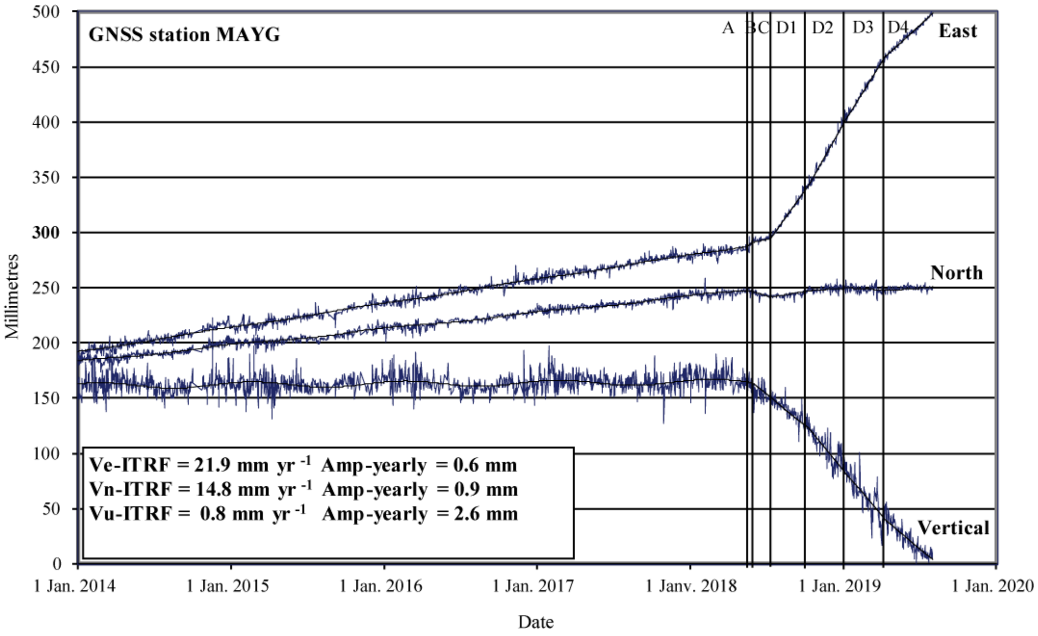

Figure 13. Full time series of station MAYG, including the evaluation of the yearly signal that must be removed to derive the real ground deformation produced by the eruption.

The time series in Fig. 14 were calculated in precise point positioning mode (PPP) with GIPSY 6.4 (from https://gipsy-oasis.jpl.nasa.gov/). They present a strong common mode, and four phases are visible: A, B, C, and D. Phase A spans from the origin of the GNSS observations (late 2013 for MAYG and early 2018 for all others) to the main earthquake of May 15th. No precursory deformation is observed at any of the stations. During phase B, from May 15th to May 30th, 2018, there is a small yet well visible deformation on the east component (Fig. 14). During phase C, from May 30th to July 3rd, there is little horizontal deformation at the stations and a slight global subsidence. During phase D, starting on July 3rd, all stations show a large and steady drift mostly east and downwards.

Table 3 contains the velocity anomalies during phase D, obtained by linear fit. The time series of the N-S component of the two southern stations, PORO and BDRL, indicate a significant northwards velocity during phase D unlike the other stations. As the E-W velocities at all stations are very similar, we averaged them and, at the first order, we consider that the average vector represents the motion of the entire island of Mayotte at the barycentre of the six points located at 45.164°E and 12.813°S. Fig. 15 shows how the pattern of the cumulated seismic moment correlates with the average eastern velocity of Mayotte.

Fig. 16 shows the evolution of the east versus north component, and east versus vertical. The figure is dominated by the large drift that occurs during phase D and shows clearly that this drift seems linear at the first order during the investigated period (early July-mid November 2018). Vertical versus east component plots for phase B, C, and D are aligned, showing that the subsidence is not restricted to phase D, but occurs also, with lower intensity, during phases B and C. For north versus east, the situation is different and phase B, C, and D occupy spaces not aligned together (top of Fig. 16).

Using the time series of Fig. 17, we estimate the best fitting velocity anomalies (thus removing the long term International Terrestrial Reference Frame (ITRF14) velocity and the yearly component of MAYG - both assumed to be valid at all stations). The velocities anomalies are summarized in Table 4.

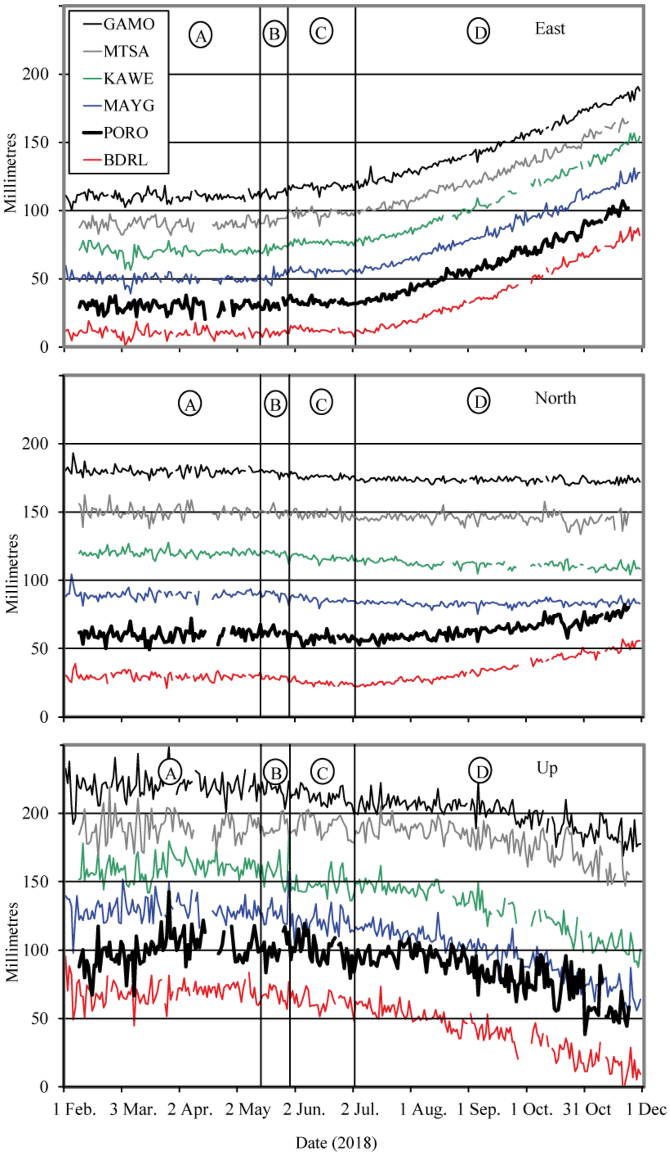

Figure 14. Time series for the coordinates of the six GNSS stations during phases A, B, C, and D, corrected for the 2014-2018 velocity, $v_E = 21.9$ mm yr^{-1} and $v_N = 14.8$ mm yr^{-1}, of MAYG.

Analysing the data until early August 2019, we split phase D in four periods of three months (D1, D2, D3, D4) in order to analyse the spatio-temporal evolution of the deformation during the eruption. Fig. 17 shows the time series at four of the GNSS stations for the period January 2018-

August 2019 (see also Fig. 13 for MAYG), which shows clearly that the deformation evolves with time and is lower rated during phases D3 and D4. Table 4 reports this observation quantitatively.

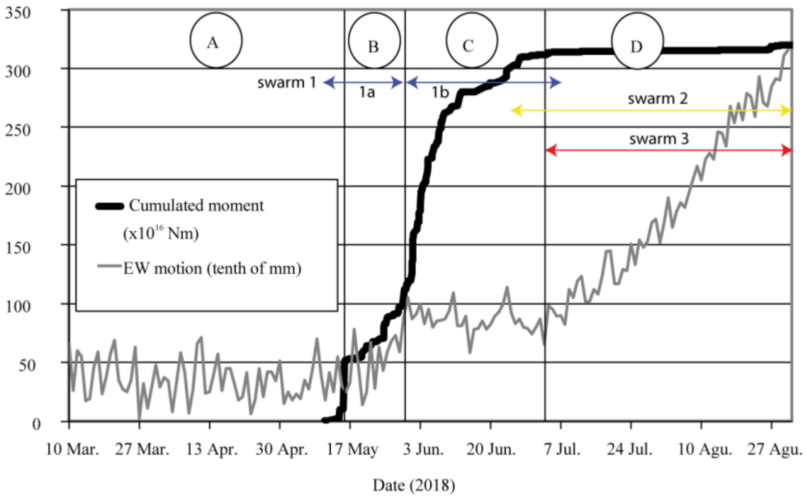

Figure 15. The phases of the crisis and the corresponding evolution of the cumulated seismic moment and average E-W displacement of Mayotte. The scale on the left is for both the deformation (mm) and the seismic moment (x 10^{16}).

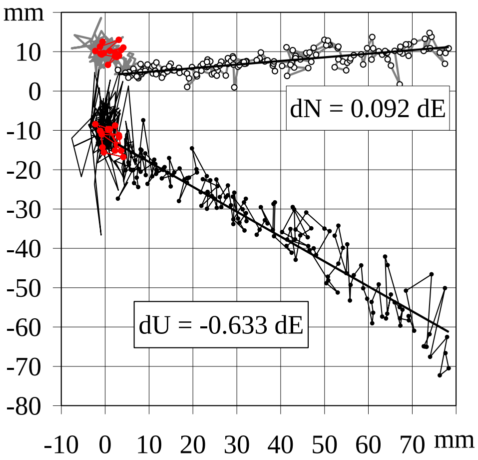

Figure 16. Ratio between horizontal and vertical motion during phase D (until mid-November 2018). For the vertical, this corresponds to a pitch of 33° between the barycentre of the six GNSS stations and the centre of the deflating source. The red dots correspond to phase B.

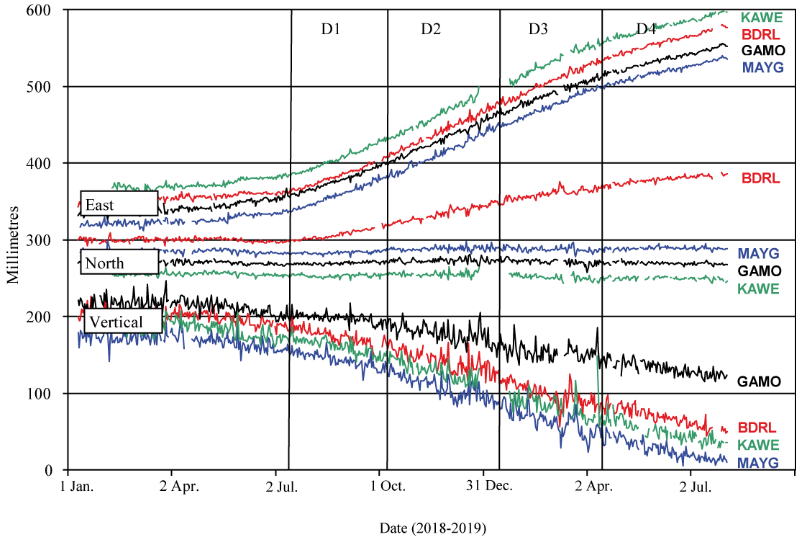

Figure 17. Time series since January 2018 at stations BDRL, GAMO, KAWE, and MAYG, with the four periods D1, D2, D3, and D4 indicated.

In order to observe the pattern of deformation for the entire Mayotte island and not only the six available GNSS stations, we performed interferometric data analysis.

5.2 Interferometric analysis

The interferometric analysis involved the processing of Copernicus Sentinel-1 mission Synthetic Aperture Radar (SAR) data from both ascending and descending acquisition geometries for the periods of December 2017 to April 2019 (29 scenes) and June 2017 to April 2019 (56 scenes), respectively. Processing was based on the Multi-Temporal SAR Interferometry (MT-InSAR) approach (Foumelis et al., 2013; Papageorgiou et al., 2019) using GAMMA software packages (Wegmüller et al., 2016). Consecutive InSAR pairs (each of the next four acquisitions, 6, 12, 18, and 24 days) were formed, and Singular Value Decomposition (SVD) was applied to solve the phase time series and corresponding displacement rates. For the purpose of the study, a single Sentinel-1 burst per satellite geometry was considered. Hence, geometric co-registration using the ALOS global digital surface model (AW3D30) of 30 m resolution, followed by cross-correlation as an enhancement step, was sufficient. Having InSAR pairs with perpendicular baselines not exceeding 150 m and an average elevation of 30 m (maximum 630 m), no major influence of topography is expected. Nevertheless, height correction, based on the correlation of interferometric phase to heights, was accounted for during processing.

InSAR measurements well-outlined the ground displacement pattern of Mayotte Island, showing a ramp subsiding East (Fig. 18), as a part of the overall concentric ground deformation common to volcano-tectonic unrests. The observed maximum rate change from one side of the Island to the other (approximately along an E-W direction) reached -115 mm yr^{-1} and -63 mm yr^{-1} for the ascending and descending tracks, respectively, which are consistent with the relative motion indicated by the GNSS network. Differences of line of sight (LoS) measurements from opposite observation points indicate the presence of significant horizontal motion, as depicted by GNSS vectors. In that case, subsidence combined with motion away from the satellite for the ascending orbit results in higher displacement rates compared to the descending one. The compatibility between InSAR and GNSS and agreement to the proposed phases of the crisis can also be seen by examining the InSAR LoS displacement time series (Fig. 18).

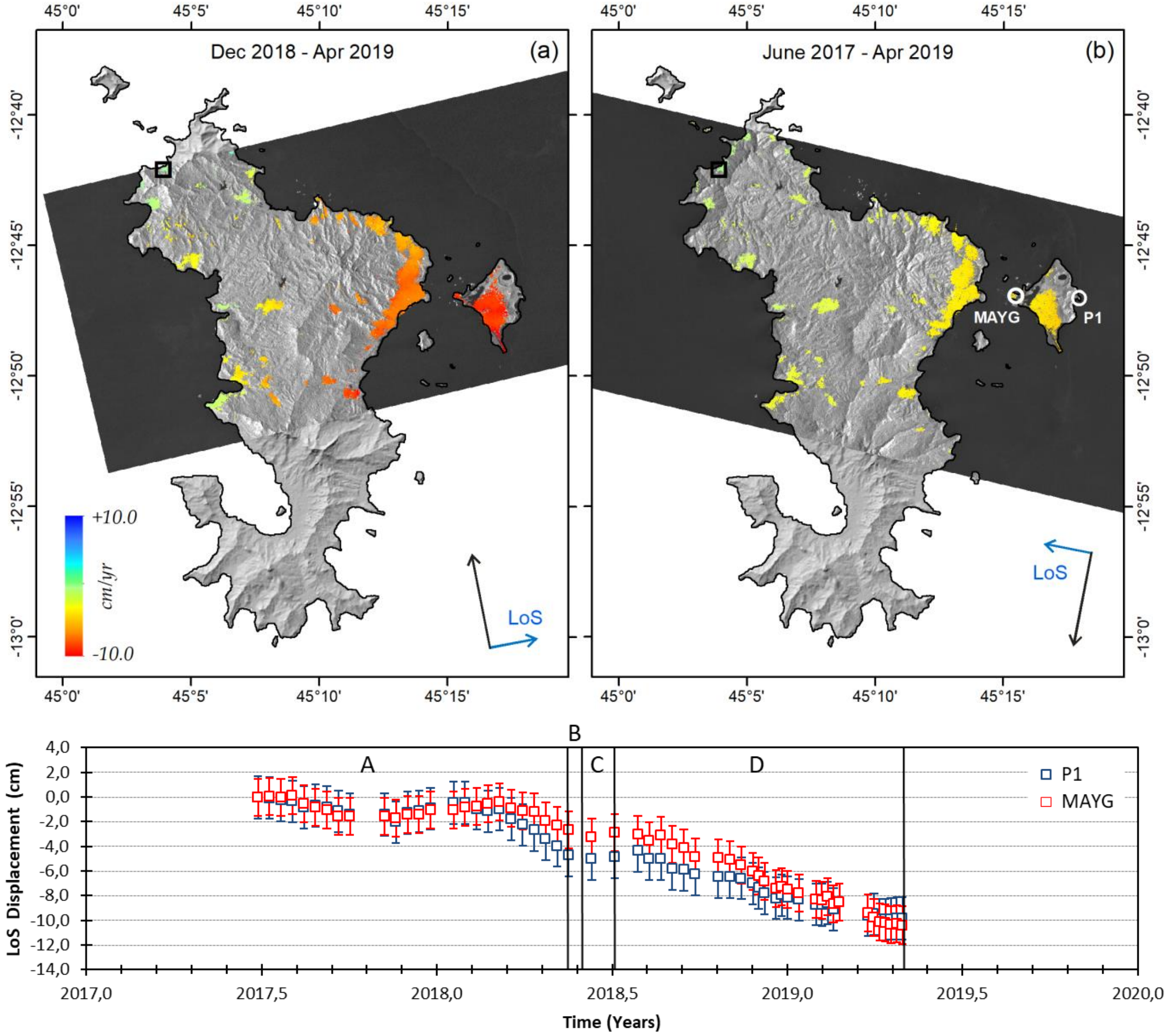

Figure 18. Sentinel-1 LoS displacement rate maps from (a) ascending and (b) descending acquisition geometries. The selected local reference is marked as a black rectangle. Displacement histories in the vicinity of the MAYG GNSS site, as well as for the easternmost point of Mayotte (white circles), together with the phases of the crisis (see text), are also shown.

It should be noted that as it is missing a region not affected by the volcano-tectonic crisis, as the entire island is deforming (GNSS observations), InSAR can provide only information regarding the relative motions within Mayotte. However, using the LoS changes estimated from the GNSS time series at nearby pixels allow us to overcome this limitation and estimate absolute LoS time series at all InSAR pixels.

Of high interest, and not achievable with GNSS, is the observation made by InSAR of the homogeneity of the displacement field within the island. The deformation pattern is affecting the whole island of Mayotte, suggesting a uniform response to the source of deformation. Nowhere in the areas sampled by InSAR can any local amplification of the ground motion be observed.

6. MODELLING THE DEFORMATIONS

6.1 Analysis of deformation pattern phases

As we have already seen, the seismicity and ground deformations are organized in four main phases. We associate them with the period preceding the seismo-volcanic phenomenon of 2018-2019 (phase A integrating current moderate seismicity and kinematics), followed by the processes of fracturing (phase B), magma ascent (phase C), and eruption (phase D). In the following, we model the ground deformations associated with phases B, C, and D.

We first model phase D, as it is the one that dominates ground deformation. We use the simple and widely used Mogi (1958) model that assumes a deflating point source buried in an elastic half space. Our data well constrain the source azimuth, pitch, and deflation, but not its distance to the stations. This is because all GNSS stations are in the same azimuth. Consequently, there is a family of solutions that fits almost equally well the data from longitude 45.55° E to longitude 45.75° E, with the source depth varying linearly from 25 to 40 km when browsing this range of solutions. If now we blend in our inversion 50% of cost of fit of the Mogi model with 50% of cost based on the crossing place of the horizontal vectors (Fig. 19), using as metrics the minimization of the cross product of the displacement vectors and the vectors source-station, we find a best fitting source at 45.590° E, 12.777° S, and 28 km depth. The corresponding emission rate is 82 $m^3 s^{-1}$ during this period, from this first analysis taking into account deflation phase D as steady between early July 2018 and mid November 2018. The blending of the two criteria in the inversion is interesting because the unconstrained Mogi modelling tends to pull the model further east (to give a better fit at one single observation, the E-W motion of MAYG, which means that these data have to be highly trusted), while the crossing of the horizontal vectors pulls the solution the other way. The combination of both gives a stable solution with mean residuals of 25, 5, and 20 mm yr^{-1} in the east, north, and vertical components, respectively (Tab. 3).

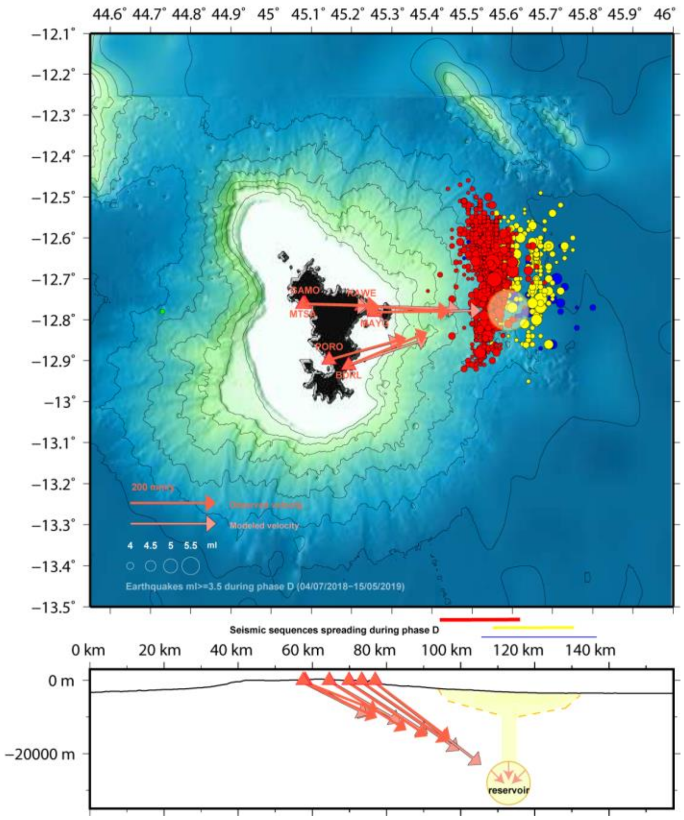

Figure 19. Orange and pink vectors are proportional to the vertical (bottom) and horizontal (top) observed and modelled velocity anomalies during phase D from July 3rd, 2018 to November 15th, 2018 (intense deflation phase), considered here to be steady. Clusters 1, 2 and 3 with $m_l > 3.5$ events from the beginning of the eruption are plotted in blue, yellow, and red (from July 4th, 2018 to May 15th, 2019). The bathymetry is from the Homonim project (SHOM, 2015) completed by Gebco_2014 data (Weatherall et *al*., 2015). Orange triangles indicate the GNSS stations. Yellow circle corresponds to the location of the magmatic chamber considered in this model (assuming a radius of 6 km), as inferred from the GNSS velocities during this phase. Yellow surfaces (bottom) represent the proposed geometry of the conduit connecting the deep reservoir to the sub-surface and potential laterally extended shallow dyke zone.

For phase C (May 30 to July 3), we interpret the deformation (Tab. 4 left) as due to the ascent of magma in a conduit connecting the deep reservoir to the sub-surface, combined with the deflation of the reservoir of a similar volume. This scenario is supported by the fact that, in that period, the E-W motion is nearly zero while there is a slight vertical motion (Fig. 14) of 7 ± 4 mm. Such ground motion can be explained with a magma body migrating upward without emission at the surface, and thus without a global volume change. As the above-mentioned subsidence rate is 55% of that of phase D and mostly attributable to the deflation of the reservoir (because a shallow source cannot produce vertical changes at GNSS stations, especially at that distance), we assume that the horizontal rate associated with the deflation is also 55% of that of phase D. This allows us to evaluate what we call the C_reservoir contribution in Tab. 4 (right). The remaining part is what we call C_conduit. We interpret it as the elastic response measured at the GNSS stations to the opening of the feeding magma conduit (Fig. 20) from the top of the chamber to the sub-surface and the further opening of shallow dykes and sills. As the emission rate is 82 $m^3 s^{-1}$ in phase D, rescaled by 55%, it is 45 $m^3 s^{-1}$ during phase C, which means that the volume injected in the channel, shallow dykes, and sills is 0.16 10^9 m^3 during phases B and C.

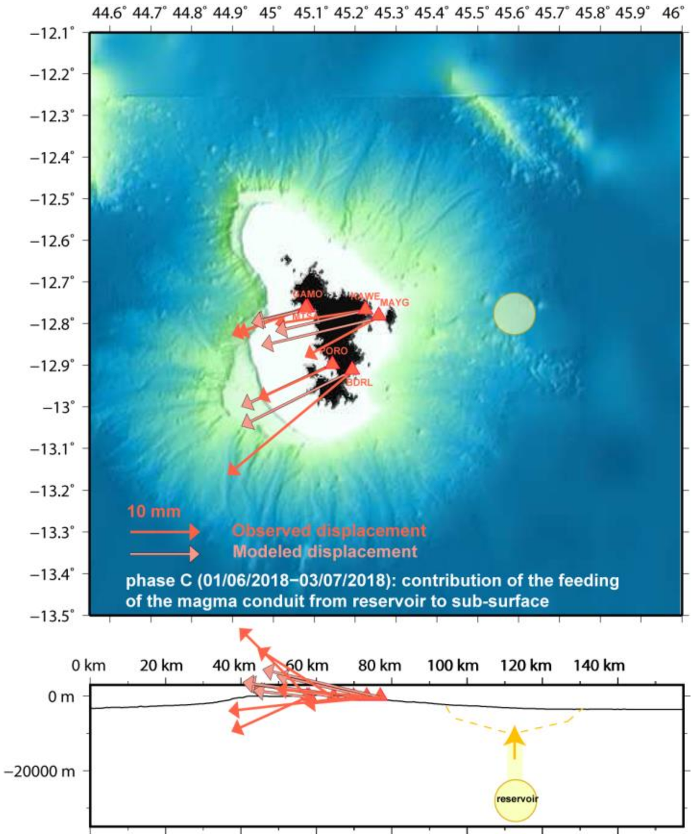

Figure 20. Same as Figure 18 (except the scale for velocities), for phase C (from June 1st to July 3rd, 2018), corresponding to the ascent of magma in a conduit connecting the deep reservoir to the sub-surface.

We model the C_conduit deformation by using the Okada (1992) formalism and the inversion code developed by Briole et al. (1986) and Briole (2017). As our GNSS stations are far from the source, we do not have a good resolution for the shape of the conduit. We assume that it is an elongated dyke buried at a depth of 22 km, at the top of a deflating chamber that we assume is 12 km in diameter (consistent with the extend of cluster 1a and with dimension of numerous well-known calderas, such as the ones reported by Geyer and Martí, 2008, e.g. Campi Flegrei in Italy) with its tip 2 km beneath the seafloor.. As a priori azimuth for the conduit, we use N304° (Section 3.3), which is perpendicular to the tension axis. The best fitting azimuth found by our inversion is N318°, though loosely constrained because of the distance of the GNSS stations. The best fitting solution for the width of the conduit is 4 ± 2 km, and its opening is 1.62 ± 0.7 m. Thus, the best fitting volume of the modelled conduit is 0.13 10^9 m^3, 20% less than the a priori value. The root mean square (rms) scatter of the residuals is 3 mm for the horizontal components and 6 mm for the vertical. In the uppermost part of the crust, the conduit could extend laterally in a shallow dyke ~20 km long, along the same axis ~N318°. This dyke could accommodate the missing 0.03 10^9 m^3.

The less active cluster 2 might correspond to earthquakes induced by redistribution of the stress in the rock surrounding the magma reservoir deflation, as it is located close to its centre (e.g., Gargani et al., 2006).

There is no means with our geodetic data to resolve precisely the characteristics of the shallow channels (dyke and or sill), because their volume is small for the distance and they do not affect the vertical component. From the vertical GNSS data, we can only assess that there cannot be a large horizontal injection at depth (e.g., 10 km long at 10 km depth) because this would give a geodetic signature that is not observed.

For phase B, during which a small yet clear deformation is observed from May 15th to May 30th, 2018, we used an Okada (1992) model with the following parameters: same location and geometry as phase C, a rectangular fault elongated vertically of 20 km length and 4 km width (Fig. 21). The best fitting slip is 0.85 m of pure strike-slip. Assuming a rigidity of $3.3\ 10^{10}$ Pa, the corresponding moment is $M = 224\ 10^{16}$ Nm, a value twice as large as the total seismic moment cumulated on May 30th, but compatible with the cumulated moment a few days later on June 2nd. When relaxing the azimuth from its initial value of N318° (inherited from phase C modelling), the best fit is obtained with N341°, which corresponds to an azimuth with the tension axis oriented at N26°, slightly smaller than those found before, but consistent with the G-CMT focal mechanisms. With both geodesy and seismology, we have no means to discriminate between the conjugate planes, and the upward fracturing during phase B might well involve ruptures that blend the two families of planes.

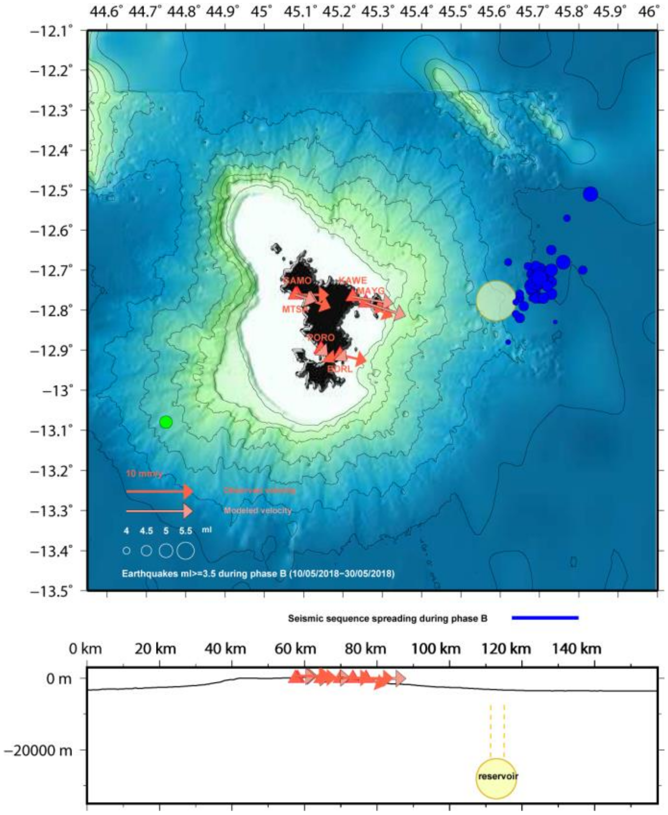

Figure 21. Same as Figure 19, for phase B (from May 10th to May 30th, 2018), corresponding to the fracturing phase.

6.2 Modelling the evolution of the deformation during deflation phase

In the previous section, we model the ground deformation measured by GNSS by using, during phase D, a single source of deformation and assuming a constant rate of deformation during period D from July 3rd until November 15th, 2018. Here, we use the available data until early August 2019 (Fig. 13 and Fig. 17), and we estimate, in four periods of three months (D1, D2, D3, and D4), the evolution of the deformation during the first year of the deflation signal. We first run our previous modelling, but for four different periods of three months each. The modelling, made by assuming the same location (horizontal and depth) of the deflating reservoir, shows a clear evolution of the effusive rate during the eruption. The rate increases during the first phase of the eruption to reach a maximum around the end of 2018. This is the period during which the largest very low frequency tremors were observed on November 11th, 2018, and during which swarms 2 and 3 reach steady activity (Fig. 3 and Fig. 4). Then, the deformation gradually decreases during the first semester of 2019 (blue line on Fig. 22), and if the same rate continues, the eruption may terminate in few months, by the end of 2019. Table 6 gives the effusive rate values for the four periods. According to that model, the total magma released from depth was 2.27 km^3 in early July 2019, one year after the start of the eruption, a value smaller than the one reported from the estimated volume of the new submarine volcanic cone discovered at the sea floor (~5 km^3, Feuillet et al., Submitted, REVOSIMA, 2019).

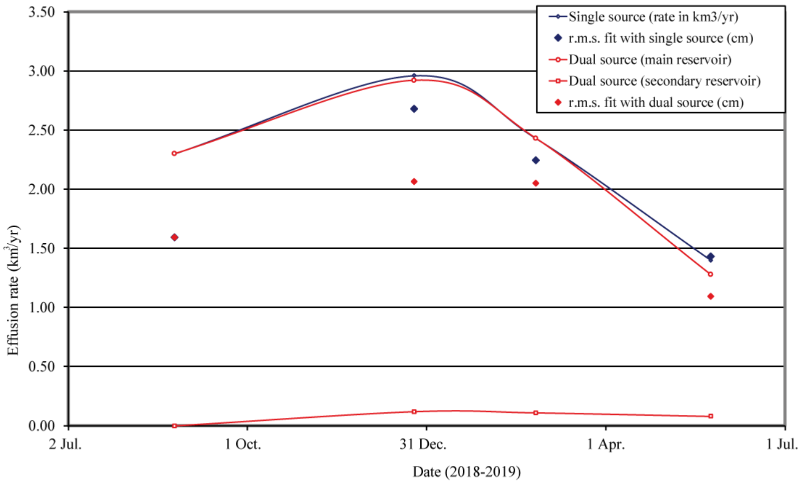

Figure 22. Temporal evolution of the deformation for single and dual source simple models.

6.3 Spatial extension of the deformation: introducing a dual source

As the GNSS time series (Fig. 13) indicate a change in deformation rate and a change of pitch (ration N-S/E-W velocities) of the deformation with time, we now introduce a dual source model in order to evaluate, at the first order with the simplest possible model, the flux of material at depth and the dynamics of the process.

Indeed, with a simple model of a unique and punctual source, the pitch is constant and gives direct information of the source azimuth (the vector points towards the source). In the case of this eruption, we see that the pitch slightly increases with time, which implies that the barycentre of the source of deformation evolves with time. The simplest way to analyse this process, with keeping the modelling approach as simple as possible in coherency with the poor coverage of the GNSS station network (and still assuming elasticity in the formal modelling), is to estimate the parameters of a secondary source that would complement the first one and provide information on the barycentre location of the deformation and its evolution. This approach is particularly valid when the secondary source is small and can be considered as a perturbation of the main one, which is indeed the case as we will see below. Considering the distribution of GNSS stations and the poor knowledge of the lithospheric structure and plumbing system, this new model cannot be considered well constrained, but should be considered as a first order model that could explain some observations.

We, therefore, introduced a second reservoir and, for each of the four phases, made a joint estimation of the horizontal location of this reservoir (assuming the depth to be the same) and the extraction rate from each of the two reservoirs. Thus, there are four parameters to be estimated for each phase (with 12 available observations).

The first important and robust result concerned the source location; the four inversions gave, in a coherent manner with differences of a few kilometres only, a location of the second source beneath the south part of Mayotte island (near station BDRL) at the best fitting location of 45.18 ° E and 12.94 ° S (Fig. 23).

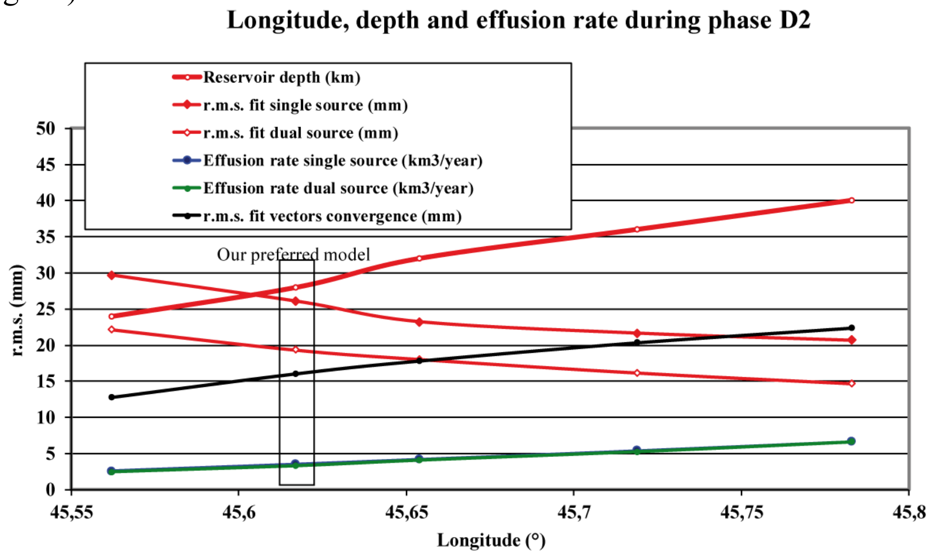

Figure 23. Parametric analysis of the depth and source type (single versus dual sources hypothesis) during phase D2.

Table 7 gives the values estimated for this dual source model. We see that the overall volume of magma released is almost unchanged with most of the magma (100% to 94%) still extracted from the main reservoir and the secondary reservoir providing a small amount of the total (0% in phase

D1, 4.1% in phase D2, 4.5% in phase D3, and 6.3% in phase D4). At the same time, this small perturbation of the model improves the fit to the data by 23%, 9%, and 24%, respectively, during phases D2, D3, and D4, which is remarkable.

It is interesting to observe that this relative amount is increasing while the total magma release is decreasing. In other words, the relative importance of this source is increasing with time.

This source might well represent (although through this coarse modelling approach) the existence of a flux of material coming from beneath the island of Mayotte (where the main asthenospheric plume leading to volcanism might be located, indicated by the location of the island on top of it) and dynamically contributing to refilling the eruptive reservoir in a process that might be regarded as an isostatic relaxation. If this is the case, despite the simplicity of our model, this model might be a good teacher for quantifying, at the first order, the volumes involved in this process, the temporal scale of this process, and the whole geometry (and complexity) of the feeding channels from beneath Mayotte island to the eruption location. Fig. 22 suggests that the eruption may terminate by the end of 2019, but there is a probability that the relaxation process inferred with source 2 might continue for some years with minor amplitude. Installing an absolute gravimeter right above the inferred secondary source might allow us to refine our understanding of this dynamic relaxation.

It should be noted that our simple dual-source approach avoids the need of invoking sources at larger depth that might be as large as 50-60 km in some models and would keep the assumption of a single source. In the next section, we discuss this question in more detail.

Finally, the fact that the dual source model predicts almost zero value of the effusion rate for the secondary source during phase D1 is an indication that this source becomes active as a response (with some delay) to the development of the eruption rather than as a trigger.

6.4 Depth of the deflation source

As mentioned above, trying to fit the GNSS data with a single source tends to lead to larger depths for the modelled sources and larger distances to the island of Mayotte. Fig. 23 and Table 8 show how the fit evolves (for both a single source and a dual source) as a function of source depth, and it is clear that deeper is better, yet just introducing the dual source leads to an equal quality of fit for a dual source at 24 km of depth or a single source at 40 km of depth. This analysis is made for phase D2 because it is the one with largest deformation. This is a clear indication that the source is not very well constrained just by the fit of the elastic modelling, nor by the poor station distribution, and a basic sophistication of the geometry can be very efficient for improving the fit. Moreover, it should be noted that, when one is looking at the horizontal vectors only, the convergence of the vectors supports a source located closer to the island at shallower depth, as shown in Fig. 23 with a “convergence” curve that corresponds to the rms of the perpendicular projection of the vectors with respect to their mean point of convergence (scalar product). We think that this refined analysis with the one year time series of data confirms and refines our initial model proposed in parallel to the identification of phases B, C, and D (from GNSS observation between the beginning in May 2018 of the unrest until November 15th, 2018). It confirms that our initial estimated depths are probably in the correct range, yet our inferred volume is less than the one inferred from the comparison of bathymetries revealed by Feuillet et al. (submitted). We may move our source slightly east by up to 5 km, thus with a reservoir depth of ~32 km, and in that case, the total volume of the released magma inferred from our dual source model would increase by ~21% and become

~2.76 km^3 for the first year of eruption, still below the ~5 km^3 inferred from the marine surveys (Feuillet et al., Submitted; REVOSIMA, 2019). The cause of this volume difference might be due to different aspects: the limitations of our model, the estimation of the volume of the new submarine volcanic cone and magmatic products, and the change of volume (and overall volumetric mass) between the material that is extracted at larger depths and the deposits near the surface. A decrease of 35-40% of the global density (thus, from 2.8 to ~2) might explain the apparent discrepancy of the volumes inferred by the two methods.

7. DISCUSSION

An intense clustering seismic sequence was analysed over a one year period, large monochromatic very low frequency seismic events were observed, and finally, patterns of ground deformation observed on Mayotte island, thanks to GNSS and InSAR data during the 2018-2019 crisis, were analysed from the beginning of the deformation observations until early August 2019 and then modelled. The recorded deformations fit the deflation model. Seismicity analysis in parallel with deformation analysis and modelling enables us to propose a scenario for the onset of a large offshore eruption, which agrees with seafloor observations presented in Feuillet et al. (submitted).

7.1 Seismological and geodetic data

At the beginning of the crisis, the seismic monitoring network was particularly inadequate, especially from May to the end of June 2018, and especially regarding azimuthal coverage and number and type of stations. It evolved during the first months, but remained particularly sparse for a year. For real-time location purposes, we arbitrary fixed event depth at 10 km in a local context where velocity models are not known. However, in May and June 2018, 350 $m_l \geq 4.0$ were detected, and the largest events could be located thanks to regional stations. Horizontal accuracy is estimated to be approximately 15 km, ranging from 10 to 20 km, depending on the available number of phases for the location. Aware of the limits of locations especially in the initial phase, station YTMZ was chosen as a reference station to refer to S-P time because it is the only local station that recorded the whole seismic sequence. However, taking account of these limitations, we could analyse the clustering aspect of the seismicity and its evolutions, and three clusters were identified.

The evolution in time and space of the ground deformation observed in Mayotte, 45 km east of the crisis, as well from GNSS and InSAR data, allows us to distinguish four phases (one before the unrest, and three phases after the beginning of the crisis corresponding to the fracturing, magma ascent, and intense deflation and eruption) and to link them to the observed seismic clusters. There is no precursory deformation before the crisis visible in the time series of MAYG (which starts in late 2013) or on the other stations (which all start in early 2018). Before the onset of the unrest, the GNSS time series show a steady displacement, which is in agreement with the InSAR time series. InSAR displacement histories imply an earlier onset of the phenomenon at the easternmost part of Petite Terre Island. This is relevant given the location of the closest GNSS station (MAYG) to the deformation source; however, such signals need to be interpreted with care as it is within the error of the solution (Fig. 18). Such observations can be proven valuable and underlines the capacity of space-borne SAR systems for monitoring purposes.

7.2 Fracturing phase and magma ascent

The intense seismic sequence began offshore Mayotte with a first cluster, active from May 10th, 2018 to early July 2018. During May 2018 (cluster 1a), intense seismicity (11 $m_l \geq 5.0$ events) is concentrated in a limited area with a diameter around 12 km. The first week of June represents the most intense week for the seismic sequence (equivalent to Mw = 6.2), and the beginning of seismicity migration towards the surface and SE until the end of June 2018 (forming cluster 1b). The migration was confirmed by G-CMT source characteristics for the largest events

The GNSS data provide information on the timing for the creation of the feeding channel that opened the way for the magma to migrate from the reservoir to the surface. This occurs during phases B and C of the deformation, between May 15th and July 3rd, 2018. Phase B, associated with moderate deformation from May 15th to May 30th, 2018, is interpreted as the fracturing phase, linked to intense cluster 1a. Moreover, the change in the deformation signature suggests that the filling of the conduit started at the end of phase B, during the peak seismicity (and rock fracturing) that occurs between May 30th and June 7th, 2018. At the same time, cluster 1b shows intense seismicity migrating upward and SE (Fig. 6 and Fig. 7) that attests to upward fracturing, while the conduit started being filled by magma until early July 2018. The fracturing of phase B can be explained geodetically without the need of filling the ruptured faults, i.e., it can be modelled thanks to coseismic displacements associated with strike-slip faulting.

We have no strong constraints on the geometry of the feeding conduit. Even a cylinder would fit the observations reasonably well. However, the best fitting model is an elongated vertical conduit starting arbitrarily at the depth of 22 km on top of the reservoir and ending at a depth of 2 km, the latter value being loosely estimated by the inversion. What is well constrained instead by the inversion, and little dependent on the shape of the source, is the volume of the conduit, 0.13 ± 0.01 10^9 m^3, and therefore, also its section, 6500 m^2. Assuming a pipe shape, its diameter would be 90 m. It is difficult to figure out how such a cylinder could appear in a few days within ~20 km of oceanic crust not having been perforated by magma in recent geological time. Therefore, it is much more likely that the feeding conduit is a dyke. The best fit for this dyke is a horizontal width of 4 km, an opening of 1.62 m, and an azimuth of N318°. The azimuth is loosely constrained because the conduit is narrow, but consistent with the overall SW-NE extension inferred from the focal mechanisms and the orientation of the extension from GNSS regional observations (Fig. 1).

The steadiness of the deformation in June 2018 implies a steady rate (within our observational uncertainties) of the magma released from the reservoir during that month. This suggests that the cracks moved towards the surface and started being filled according to a relatively smooth process.

The G-CMT focal mechanisms are associated with the largest events of May and June 2018. Those events belonging to cluster 1, during which there is an apparent ~10 km SE epicentral migration (Fig. 6). This migration, potentially an artefact due to the assumption of uniform 10 km depth for all events and the sparse network, was confirmed by location of the largest events by G-CMT (Fig. 7). However, there is evidence of upward migration: The event depths determined by G-CMT show a clear upward migration from early to late June 2018 (Fig. 7). During the 2011-2012 El Hierro unrest, a migration extending over 20 km and ending in an offshore eruption was precisely located (López et al., 2012; Martí et al., 2013). White and McCausland (2016) compiled data from high-frequency swarms linked to eruptions and intrusions. They noticed that, generally, seismicity began at a distance that can reach tens of km from the eruptive location.

Focal mechanisms (G-CMT) show the dominance of strike slip events during the fracturing period. In Fig.5, the strike-slip focal mechanism represents earthquakes belonging to the period from May 14th to June 27th, 2018, i.e., corresponding to deformation phases B (fracturing) and C (magma ascent). Dyke related seismicity also sometimes produces the so called "dogbone seismicity distribution", where normal faulting events around the dyke (normal faults parallel to dyke) coexist with strike slip events around it (e.g., Toda et al., 2002). In the case of the Mayotte seismo-volcanic phenomenon, only the largest events are associated with a focal mechanism, leading to a lack of accuracy in the description of the seismicity pattern.

We interpret cluster 1 as corresponding to fracturing and magma ascent. The seismicity for the first period of cluster 1 (cluster 1a, fracturing phase) is expected to be roughly superimposed with the location of the reservoir, before beginning the upward and SE migration in early June 2018 (cluster 1b, magma ascent). This preliminary interpretation permits us to propose a rough location correction corresponding to the location bias between cluster 1a and the position of the reservoir: i.e., ~14 km W and ~6 km S. This shift is large, but within the error bars of the localisation of the events, given the weakness of the network and the standard velocity model that has been used while not necessarily adequate for the situation. In Fig. 24, we moved, following the above shift, the centres of clusters 1a and 1b (determined thanks to ml ≥ 4.5 earthquake locations). We assume that this might represent the best compromise between the constraints from the geodetic modelling and the uncertainties in the localisation of the seismicity. The submarine eruptive observations highlighted in May 2019 during MAYOBS campaigns (doi: 10.18142/291; 10.17600/18001222; 10.17600/18001230; 10.17600/18001238) support the proposed interpretation regarding cluster 1: during June 2018, beginning with a very intense seismic phase, upward and SE migration was observed until the end of June before the eruption began in early July 2018 (Fig. 24).

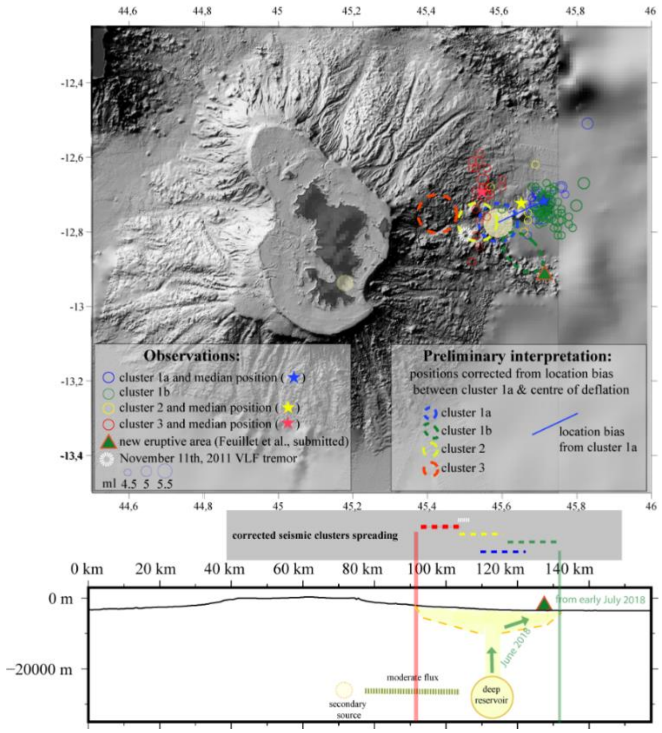

Figure 24. Yellow full filled circle represents the main reservoir inferred by the GNSS data. Small open circles represent seismicity (ml >4.5), and large opened dashed areas represent the preliminary interpretation regarding the position of the centres of the three clusters shifted 14 km westward and 6 km southward with respect to their native location, so as to bring geodesy and seismology results closer, within their respective uncertainties. This shift corresponds to the bias between the centre of deflation deduced by GNSS data and the centre of cluster 1 during the fracturing phase B, i.e., before the upward and southeast migration of the magma. The eruption takes place on the green triangle, as observed during marine surveys (Feuillet et *al.*, submitted). It is connected to the vertical conduit by a ~20 km long dyke. The bathymetry is from SHOM (Homonim project) and Gebco_2014 (Weatherall et *al.*, 2015). The model includes a main deep reservoir and a secondary source beneath the south end of Mayotte island.. A moderate flux of material (~3 m^3s^{-1}) is inferred from that source to the main reservoir. Vertical green and red lines delimit area of active seismicity during the first year of the sequence.

7.3 Intense deflation

A second seismic cluster, much less active than the first one, appears at the end of June 2018, centred WNW in comparison with the first cluster. It occurred during a short intense period of seismicity (end of June 2018), marking the last stage of migration. Then, seismicity began a period of quiescence in July and August 2018. During this period, a third cluster began in early July 2018, again centred WNW in comparison to the second cluster. The second and third clusters are still active at the time of this paper, but the seismicity of the third one remains more intense.

In parallel, during early July 2018, the deformation pattern observed at GNSS stations changed and presented large eastward and downward drifts. We interpret this signal as the beginning of the offshore eruption. We modelled this phase of intense deformation with a source of deflation.

Moreover, cluster 2 appeared at the end of the migration phase, i.e., the end of June 2018, and remained active until now. Just after the beginning of the eruption, during the period of seismic quiescence, the third cluster appeared. It is the closest to Mayotte island and the most intense. Both clusters 2 and 3 present b-values higher than the one of cluster 1, which is consistent with values observed at some volcanoes (e.g., Wyss et al., 1997).

Because of the poor azimuth coverage of the GNSS stations (Fig. 19), the longitude of the deflation source is not easy to assess. However, as our two criteria (best fitting Mogi source and horizontal crossing of the vectors) are leading in opposite directions, we believe that our localisation of the deflating source is resolved within a few kilometres in a robust way. Subsequently, its depth (28 km) is constrained accurately by the pitch of the deformation and the trade-off between distance and depth in the model (Fig. 23). Its azimuth is well constrained by the azimuths of the GNSS vectors. A similarly deep magmatic reservoir can be found in El Hierro (~25 km, Martí et *al*., 2013, Klügel et *al*., 2015) or in the Klyuchevskoy volcano group in Kamchatka (z~30 km, Levin et *al*., 2014; Shapiro et *al*., 2017), linked to shallower sources.

Our modelling assumes that the source is a point, which is of course not the case, but we cannot resolve this with GNSS network as, at such distance, a source with a radius of several kilometres is indistinguishable from a point source. We assumed that the source diameter is 12 km, because this is a typical value used in literature for deep reservoirs, based on the size of many calderas that can be seen on Earth (e.g., the Campi Flegrei caldera in Italy as described in the database from Geyer and Martí, 2008). It also ranges with the dimension of the area where earthquakes of cluster 1a were concentrated (interpreted as the fracturing phase preceding any magma ascent).

The rate of magma released is less in June, approximately half, than the one estimated after July 3rd, 2018. In other words, the flux in the feeding channel doubled in July once the path to the surface opened, and the eruption started. The timing of the start of the eruption, estimated on July 3rd, 2018, comes from the beginning of the large ground deformations, thus, when there is no longer a balance between the volumes collected at large depth in the reservoir and those stored at shallow depth. With 6500 m^2 for the best fitting section of the feeding channel and 82 $m^3 s^{-1}$ for the effusive rate, if we consider a constant emission rate between July 3rd and November 15th, 2018, the speed of magma ascent is 0.013 $m s^{-1}$. The speed was half this rate between May 30th and June 30th, 2018, when migration of seismicity revealed the magma migration (during June 2018). Such a low speed of magma ascent has been observed elsewhere and is discussed by Gonnermann & Manga (2013) through the analysis of the crystals in the erupted magmas.

The GNSS time series during this deflation phase evolves with time. Assuming a constant position of the deflating reservoir, it induces an evolution with the effusion rate predicted by the model. It first increased through late 2018, then decreased. This phase of deformation is still active at the date of this paper, more than one year after the eruption began.

With an effusion rate of 45 $m^3 s^{-1}$ over 42 days (magma ascent phase C) and then, after the estimated beginning of the eruption early July 2018, four phases over three months with rates 72.9, 93.8, 77, and 44.4 $m^3 s^{-1}$, the total volume extracted from the chamber is 2.43 km^3, according to our modelling. White and McCausland (2016) proposed an empirical tool for estimating the intruded magma volume from the analysis of a large range of past high-frequency earthquake swarms that preceded past eruptions or intrusions. Considering the cumulative seismic moment between May 10th, 2018 and May 15th, 2019, the estimated magma volume should be of the order of 1.55 km^3, lower than what we predict at this date from GNSS data (~2.21 km^3). Moreover, recent marine surveys (R/V Marion Dufresne) performed bathymetric and water column observations that confirm recent submarine volcanic activity, 50 km eastward from Mayotte, and differential bathymetry allowed to estimate an important volume emitted at the seafloor of ~5 km^3 (Feuillet et al., submitted; REVOSIMA, 2019). The volume of released magma from the reservoir that we estimated is much lower than the volume deduced from direct seafloor observations of the eruption. This discrepancy can have different origins, including potential volume change of material between its extraction at 28 km depth and the seafloor. Moreover, our model presents several limitations, among them the hypotheses of elasticity and point sources. However, it is a major eruption with exceptional volume and an effusive rate that can be compared to very large eruptions such as the Lanzarote one between 1730 and 1736, that emitted 3-5 km^3, associated with an effusion rate five times lower than the one estimated for Mayotte with comparable volumes (Carracedo et al., 1992). The Laki eruption spanned from June 1783 to February 1784 and emitted 14.7 km^3 of magma, with an effusive rate nearly four times higher than the one from Mayotte (Thordarson and Self, 1993).

In order to explain the observed pitch of the deformation, a simple dual source model is proposed, assuming the depth of the secondary source to be the same as that of the main one. Location and extraction rate are inverted for four periods of three months each for each reservoir. Introduction of this second source improves the fit between model and observations by ~20%. From geodetic data analysis, Bato et *al.* (2018) proposed deep connections between the two volcanic systems of Grímsvötn and Bárðarbunga (Iceland), ~25 km away explained by lateral flow hypothesis at depth or shared magma reservoir at depth ~30 km. From the 2011-2012 submarine El Hierro eruption analysis, Klügel et al. (2015) suggested that lateral magma movements at depth are typical of mature oceanic intraplate volcanoes. They proposed that between 2011 and 2014, pre-, syn- and post-eruptive seismic swarms testify to the presence of magma paths in the uppermost mantle and lower crust. For Mayotte, models will evolve as supplementary data arrives (from new GNSS stations installation and marine surveys).

Phase D of intense deflation, which has run for more than one year at the time of this paper, is the phase with the lowest seismic rate. This indicates that the fracturing from the reservoir depth to the subsurface is terminated. Applying, to the first order, the correction for the location deduced from the coupled analysis of seismicity and deformation during cluster 1, the centre of the second cluster, which spans from the end of June 2018 until now, is located in the vicinity of the deflation centre. During the El Hierro eruption (2011-2012), Martí et al. (2013) interpreted the syn-eruptive seismicity as a response to readjustments of the plumbing system following magma withdrawal. As the plumbing system in the case of Mayotte is not described, it is difficult to propose a reliable explanation for the sources of clusters 2 and 3, both of which are syn-eruptive. A new swarm or geometry in the seismicity pattern can mark changes in magma circulation (e.g., segmented dyke growth in 2014 in the Bárðarbunga volcanic system, Sigmundsson et al., 2015). In the present case, it seems that there is no link between clusters 2 and 3, except that they are both syn-eruptive. Cluster 2, due to its vicinity with the centre of deflation, should be linked to the redistribution of stress around the reservoir due to magma withdrawal. Moreover, the third cluster could be linked to fluid movement maybe between the two reservoirs. The lateral flow hypothesis that would permit a connection between volcanic systems at depth should be associated with an increase in seismicity (Bato et al., 2018).

7.4 November 11th, 2018 very low frequency tremor

On November 11th, 2018, a very low frequency monochromatic long lasting tremor, associated with a period of ~16 s, was recorded worldwide by broad-band stations. It was emitted from the active area east of Mayotte, close to cluster 3 (Fig.11). This event presents some similarities with two events reported in Polynesia by Talandier et al. (2016). They explained these events as a resonance of a fluid filled reservoir induced by magma movement under high hydrostatic pressure. If this event belongs to VLP seismicity (regarding frequency range), its waveforms are typical of some LP events associated with the decaying oscillation in a resonator. As with the events reported in 2011 and in 2013 in Polynesia by Talandier et al. (2016), the November 11th, 2018 event and other smaller ones generated offshore Mayotte can be considered as endmember seismic events due to oscillation after punctual excitation. The source process is non-destructive as several events with the same characteristics were observed. Potential sources for such events that present similarities with the November 11th, 2018 event, especially regarding a very low oscillation frequency range or oscillating pattern, could be fluid-filled cracks pressurized in a hydrothermal system (e.g., Aso volcano, Hendriyana et al., 2019), basaltic magma in a dike (e.g., Kumagai et al., 2003) or magma movement inducing resonance within a shallow opened conduit under high hydrostatic pressure (Talandier et al., 2016). The constraints on the geometry of the deep feeding channel, and a possible shallow dyke, can be used as a priori geometric model for the interpretation and modelling of the reported low frequency tremors. Those could be generated by an oscillation, potentially in a long horizontal shallow dyke or in the magma reservoir, but not in the vertical conduit as the particle motion does not support the hypothesis of a vertical vibrating source.

Constraining the source of November 11th, 2018 does not belong to the objectives of this work, but future analysis of this unusual event could help us understand plumbing systems and resonating fluid characteristics.

7.5 Mayotte 2018-2019 seismo-volcanic sequence

The centre of cluster 3 is ~20 km from the centre of cluster 1 in the azimuth N305°, aligned roughly with cluster 2. The three seismic swarms show an overall migration of activity WNW, indicating a coaxial complex and extended activity. Nearly all focal mechanisms made by G-CMT indicate an extension axis oriented ~N50°. The perpendicular azimuth N310° is therefore the most favourable axis for a feeding dyke, and thus, close to the abovementioned N305°. This azimuth is consistent with some topographic features observed in the bathymetry east of Mayotte, e.g., the Jumelles seamounts (NE from Mayotte, Fig.1), and with that of dykes exposed onshore north of Mayotte (Nehlig et al., 2013). It is also consistent with the overall axis of the Comoros volcanic Archipelago and is roughly perpendicular to the relative motion measured by GNSS (Fig. 1) in azimuth N50° across the Comoros. It is possible that some ancient structures were reactivated and opened to give way to the rising magma. Active structures are not identified around Mayotte

The 2018 Mayotte crisis shows some similarities with past telluric crises involving dyke intrusions. For example, Ahmed et al. (2016) suggested a diking event related to intense seismicity involving 29 M > 5.0 earthquakes in the Gulf of Aden over a few months, where seismic migration is interpreted as magma ascent before dike propagation. As in the case of Mayotte, cluster 1b may correspond to a phase of shallow injection (upward and lateral migration). Regarding the reservoir depth (25 km) or distance of migration, the Mayotte seismo-volcanic crisis shares many similarities with that of 2011-2012 at El Hierro, Canary Island, where the activity was characterised by several phases, including phases of migration and submarine eruption (e.g., Martí et al., 2013).

However, our models are only first order models that explain seismicity and deformation pattern during the seismo-volcanic crisis of Mayotte and build a scenario for the onset of a large eruption.

8. CONCLUSIONS

The combined analysis of the spatio-temporal evolution of seismicity and deformation (from GNSS and InSAR observations) allows us to propose a first order scenario regarding the seismo-volcanic phenomenon from an intense seismic sequence beginning on May 10th, 2018 to the discovery of a new offshore volcanic edifice just one year later (Feuillet et al., submitted).

During this seismo-volcanic phenomenon, we identified three distinct seismic swarms, clustering in space and time and marking an overall WNW migration, which are also linked to three phases of ground displacement. The first swarm spanned from May 10th and the beginning of July 2018. It included the largest events recorded during the whole crisis (29 among the 32 ml ≥ 5.0 events reported), and even the largest earthquake ever recorded in Comoros (Mw = 5.9 on May 15th, 2018). The first weeks (May 10th-May 31th 2018) were interpreted as a phase of upward fracturing. Intense seismicity was associated with a small GNSS signal modelled as coseismic displacement due to strike-slip faulting. The second part of this first swarm, covering June 2018, began with a week of very intense seismicity (equivalent to Mw = 6.2) and was characterized by seismic migration SE and towards the surface. This period is linked to another phase of deformation due to magma ascent between a deep reservoir and the sub-surface. After another period of relatively intense seismicity marking almost the end of the first swarm (end of June 2018), on one hand, a period of seismic quiescence began for 2 months, and on the other hand, GNSS and InSAR data showed large eastward and downward drift from July 3rd, 2018. We interpret this date as the beginning of an eruption.

Since July 3rd, 2018, the ground displacement pattern is explained by a model considering the deflation of a reservoir centred at 28 km depth and characterized by an estimated diameter of 12 km roughly located 30 km east of Mayotte. More than one year after the beginning of this deflating phase, drift is still active, and the area east of Mayotte has subsided by around 0.15 m and moved eastward by around 0.2 m.

A second swarm began at the end of June, mostly WNW from the first swarm and close to initial events of the first swarm. Its activity is moderate in comparison with the first swarm, but it has been active during the whole period of observation. It is interpreted as caused by accommodation of the whole system surrounding the deflating reservoir due to stress changes linked to the withdrawal of magma. The third seismic swarm initiated almost at the same time as the beginning of the deflation, WNW from the second swarm. This third swarm is more active than the second one and was still active at the end of the observation period. It is more difficult to interpret without complementary data, but it may be the signature of magma connection between different reservoirs

A long-lasting (more than 20 mn) and intense monochromatic very low frequency (~0.062 Hz) seismic event that occurred on November 11th, 2018 is also a sign of active magmatic process. It was roughly located next to cluster 3. Other events, weaker, but with similar characteristics, occurred, suggesting a common source and a non-destructive process. Such an intense very low frequency harmonic oscillation of a fluid filled resonator is unusual and could be attributed to punctual excitations due to fluid movement and hydrostatic pressure conditions.

Between early July 2018 and April 2019, the deformation presents a quite homogeneous strong signal. However, the year of deflation was divided into four phases, showing an evolution of the effusive rate during the eruption. It increased until reaching a maximum value around the end of 2018 (93.8 $m^3s^{-1)}$ and then decreased gradually. Between October 2018 and April 2019, a sustainable seismicity was observed, essentially regarding cluster 3. At the end of April 2019, seismicity entered a slowdown phase. The total magma released from depth, according to our model, is estimated between 2 and 3 km^3. If the current behaviour continues, the eruption could end around late 2019.

Whereas the plumbing system and local structure are still unknown, adding a smaller secondary source of deflation improves the modelling of the GNSS signal. Such a simple model implies a moderate flux transfer between the secondary source and the main one, which may be the cause of the third seismic swarm.

The seismo-volcanic crisis of 2018-2019 offshore Mayotte has shown activity of a WNW-ESE aligned system. It marks the end of a period of quiescence several ky in length of the Mayotte island edifice and occurred in a poorly known and poorly instrumented area. However, it confirms the alignment of active seismicity and volcanism around Comoros archipelago, between the Somalian plate and Lwandle block in an extensive regional context, consistent with trans-tensional regime in the area. The ongoing crisis in Mayotte might be important for teaching us more about the dynamics of the extension between the Somali plate and the Lwandle block and the related volcanism. Improving this knowledge and improving the knowledge of the distribution, alignment, and ages of the offshore volcanic features, especially around the main islands, may lead to a better understanding of the behaviour, evolution, and related hazards of this peculiar area.

ACKNOWLEDGEMENTS

We are grateful to Jean Battaglia, Julien Bernard, Nicolas Chamot-Rooke, Alison Colombain, Christine Deplus, Andrea Di Muro, Cécile Doubre, Rémi Dretzen, Valérie Ferrazzini, Nathalie Feuillet, Bruno Garayt, Cécile Gracianne, Marc Grunberg, Roser Hoste Colomer, Eric Jacques, the Gempa team, the Guralp hotline, Philippe Jousset, Philippe Kowalski, Frédéric Lacquement, Jérôme Lambert, Yohann Legendre, Arnaud Lemarchand, Hélène Lyon-Caen, Estelle Maisonneuve, Kristel Meza Fajardo, Fabien Paquet, Aline Peltier, Sébastien Saur, Jean-Marie Saurel and Jérôme van der Woerd for their help and the fruitful discussions. IPGP and RéNaSS performed the observatory work during August 2018. Didier Bertil reprocessed the initial locations and magnitudes. IPGP shared the data from Grande Comore. IGN/RGP and its partners TERIA, Lél@sarl, and CNES provided the GNSS data, RESIF-RAP network hosted the YTMZ accelerometer (RESIF is a national Research Infrastructure, recognised as such by the French Ministry of Higher Education and Research. RESIF is managed by the RESIF Consortium, composed of 18 Research Institutions and Universities in France. RESIF is additionally supported by a public grant overseen by the French National Research Agency (ANR) as part of the "Investissements d'Avenir" program (reference : ANR-11-EQPX-0040) and the French Ministry of Ecology, Sustainable Development and Energy), EDUSISMO was responsible for the existence of the station MCHI and ISC for its catalogue of seismicity. This study was funded by BRGM and French Ministry MTES/DGPR. We used the software GMT to produce maps (Wessel & Smith, 1995), SAC, Seiscomp, GIPSY Oasis 6.4 and bathymetric data from Homonim project (SHOM, 2015), and Gebco_2014 (Weatherall et al., 2015). Author contribution statement: D.B. built the

monitoring tools, D.B., A.R., and A.L. analysed the seismological data, P. V. performed GNSS computations, P.B. analysed the GNSS data and made the deformation model, M.F. performed InSAR data analysis, assisted by M.M and D. R., I.T. brought her knowledge on the local context, and P.B. and A.L. wrote the paper.

REFERENCES

Ahmed, A., Doubre, C., Leroy, S., Kassim, M., Keir, D., Abayazid, A., Perrot, J., Audin, L., Vergne, J., Nercessian, A., Jacques, E., Khanbari, K., Sholan, J., Rolandone, F. & Al-Gand, I., 2016. Seafloor spreading event in western Gulf of Aden during the November 2010–March 2011 period captured by regional seismic networks: Evidence for diking events and interactions with a nascent transform zone, *Geophysical Journal International*, **205**(2), 1244-1266.

Aki, K. and P. G. Richards. Quantitative Seismology. University Science Books, 2nd edition, 2002.

Audru, J. C., Guennoc, P., Thinon, I. & Abellard, O., 2006. Bathymay: la structure sous-marine de Mayotte révélée par l'imagerie multifaisceaux, *Comptes Rendus Geoscience*, **338**(16), 1240-1249.

Ayele, A., Jacques, E., Kassim, M., Kidane, T., Omar, A., Tait, S., A. Nercessian, J.-B. de Chabalier & King, G. (2007). The volcano–seismic crisis in Afar, Ethiopia, starting September 2005. *Earth and Planetary Science Letters*, **255**(1-2), 177-187.

Bassias, Y., & L. Leclaire, 1990, The Davie Ridge in the Mozambique Channel: crystalline basement and intraplate magmatism, Neues Jahrbuch für Geologie und Paläontologie, **4**, 67–90.

Bato, M. G., Pinel, V., Yan, Y., Jouanne, F., & Vandemeulebrouck, J. (2018). Possible deep connection between volcanic systems evidenced by sequential assimilation of geodetic data. *Scientific reports*, **8**(1), 11702.

Battaglia, J., Ferrazzini, V., Staudacher, T., Aki, K., & Cheminée, J. L., 2005. Pre-eruptive migration of earthquakes at the Piton de la Fournaise volcano (Réunion Island). *Geophysical Journal International*, **161**(2), 549-558.

Bertil, D. & Regnoult, J.M., 1998, Seismotectonics of Madagascar, *Tectonophysics*, **294**, 57–74.

Bertil, D, Roullé, A, Lemoine, A, Colombain, A, Maisonhaute, E & Dectot., G, 2018. MAYEQSwarm2018 : BRGM earthquake catalogue for the Earthquake Swarm located East of Mayotte. May 10th -November 12th, 2018, https://doi.org/10.18144/372c5809-3d30-440c-b44a-1c89385f176a

Bertil, D., Roullé, A.,Lemoine, A., Colombain, A., Hoste-Colomer, R., Gracianne, C., Meza-Fajardo, K., Maisonhaute, E., Dectot, G., 2019. MAYEQSwarm2019 : BRGM earthquake catalogue for the Earthquake Swarm located East of Mayotte.2018 May 10th - 2019 May 15th, https://doi.org/10.18144/rmg1-ts50.

Blewitt, G., Hammond, W.C. & Kreemer, C., 2018. Harnessing the GPS data explosion for interdisciplinary science, *Eos*, **99**, https://doi.org/10.1029/2018EO104623.

Briole, P., De Natale, G., Gaulon, R., Pingue, F. & Scarpa, R., 1986. Inversion of geodetic data and seismicity associated with the Friuli earthquake sequence (1976-1977), *Annales Geophysicae*, **4**(B4), 481-492.

Briole, P., 2017. Modelling of earthquake slip by inversion of GNSS and InSAR data assuming homogenous elastic medium, *Zenodo*. http://doi.org/10.5281/zenodo.1098399

Calais, E., Ebinger, C., Hartnady, C. & Nocquet, J.M., 2006. Kinematics of the East African Rift from GPS and earthquake slip vector data, *Geological Society, London, Special Publications*, **259**(1), 9-22.

Carracedo, J. C., Badiola, E. R., & Soler, V., 1992. The 1730–1736 eruption of Lanzarote, Canary Islands: a long, high-magnitude basaltic fissure eruption. *Journal of Volcanology and Geothermal Research*, 53(1-4), 239-250.

Chouet, B. A. (1996). Long-period volcano seismicity: its source and use in eruption forecasting. *Nature*, **380**(6572), 309.

Chouet, B., 2003. Volcano seismology. Pure and Applied Geophysics, 160(3-4), 739-788.

Chouet, B. A., & Matoza, R. S., 2013. A multi-decadal view of seismic methods for detecting precursors of magma movement and eruption. *Journal of Volcanology and Geothermal Research*, **252**, 108-175.

Daniel, J., Dupont, J. & Jouannic, C., 1972. Relations Madagascar-archipel des Comores (Nord-Est du canal de Mozambique): sur la nature volcanique du Banc du Leven, *Comptes Rendus de l'Académie des Sciences. Série D: Sciences Naturelles*, **274**(12), 1784-1787.

Davis, J.K., Lawver, L.A., Norton, I.O. & Gahagan, L.M., 2016. New Somali basin magnetic anomalies and a plate Model for the early Indian ocean, *Gondwana research*, **34**, 16–28. Https://doi.org/10.1016/j.gr.2016.02.010

Debeuf, D., 2004. Etude de l'évolution volcano-structurale et magmatique de Mayotte, Archipel des Comores, océan Indien: approches structurales, pétrographique, géochimique et géochronologique, PhD, La Réunion University, 277p.

DeMets, C., Gordon, R.G. & Argus, D.F., 2010. Geologically current plate motions, *Geophysical Journal International*, **181**(1), 1-80.

Delvaux, D. & Barth, A., 2010. African stress pattern from formal inversion of focal mechanism data, *Tectonophysics*, **482**, 105-128.

Déprez, A., Doubre, C., Masson, F. & Ulrich, P., 2013. Seismic and aseismic deformation along the East African Rift System from a reanalysis of the GPS velocity field of Africa, *Geophysical Journal International*, **193**(3), 1353-1369.

Deville, E., Marsset, T., Courgeon, S., Jatiault, R., Ponte, J. P., Thereau, E., Jouet, G., Jorry, S. J. & Droz, L., 2018. Active fault system across the oceanic lithosphere of the Mozambique Channel: Implications for the Nubia–Somalia southern plate boundary. *Earth and Planetary Science Letters*, **502**, 210-220.

Dziewonski, A.M., Chou, T.A. & Woodhouse, J.H., 1981. Determination of earthquake source parameters from waveform data for studies of global and regional seismicity, *J. Geophys. Res.*, **86**, 2825-2852, doi:10.1029/JB086iB04p02825.

Edusismo, http://www.edusismo.org

Ekström, G., Nettles, M. & Dziewonski, A.M., 2012. The global CMT project 2004-2010: Centroid-moment tensors for 13,017 earthquakes, *Phys. Earth Planet. Inter.*, **200-201**, 1-9, doi:10.1016/j.pepi.2012.04.002.

Emerick, C.M. & Duncan, R.A., 1982. Age progressive volcanism in the Comores Archipelago, eastern Indian Ocean and implications for Somali plate tectonics, *Earth Planet Sci Lett* **60**(3), 415–428.

Feuillet, N., Jorry, S. J., Crawford, W, Deplus, C. Thinon, I, Jacques, E. Saurel, J.M., Lemoine, A., Paquet, F., Daniel, R., Gaillot, A., Satriano, C., Peltier, A., Aiken, C., Foix, O., Kowalski, P., Laurent, A., Beauducel, F., Grandin, R., Ballu, V., Bernard, P., Donval, J.P., Geli, L., Gomez, J. Guyader, V., Pelleau, P., Rinnert, E., Bertil, D., Lemarchand, A., Van der Woerd, J., 2019. Birth of a large volcano offshore Mayotte through lithosphere-scale rifting, submitted to *Nature*.

Flower, M. F. J., & Strong, D. F., 1969. The significance of sandstone inclusions in lavas of the Comores Archipelago, *Earth and Planetary Science Letters*, 7(1), 47-50.

Foumelis, M., Trasatti, E., Papageorgiou, E., Stramondo, S. & Parcharidis, I., 2013. Monitoring Santorini Volcano (Greece) breathing from space. *Geophysical Journal International*, doi: 10.1093/gji/ggs135.

Gargani, J., Geoffroy, L., Gac, S., & Cravoisier, S., 2006. Fault slip and Coulomb stress variations around a pressured magma reservoir: Consequences on seismicity and magma intrusion. Terra Nova, 18(6), 403-411.

GEOFON Data Centre, 1993. GEOFON Seismic Network. Deutsches GeoForschungsZentrum GFZ. Other/Seismic Network. doi:10.14470/TR560404.

Gevrey A., 1870. Essai sur les Iles Comores. Editeur A. Saligny (Pondichéry). 307 p., ark:/12148/bpt6k62208586

Geyer, A., & Marti, J., 2008. The new worldwide collapse caldera database (CCDB): A tool for studying and understanding caldera processes. *Journal of Volcanology and Geothermal Research*, **175**(3), 334-354.

Gómez M, D. M., & Torres C, R. A., 1997. Unusual low-frequency volcanic seismic events with slowly decaying coda waves observed at Galeras and other volcanoes. *Journal of volcanology and geothermal research*, **77**(1-4), 173-193.

Gonnermann, H.M. & Manga, M., 2013. Dynamics of magma ascent in the volcanic conduit, in Modeling Volcanic Processes, The Physics and Mathematics of Volcanism, eds. Fagents, S.A., Gregg, T.K.P. and Lopes, R.M.C., *Cambridge University Press, Cambridge*.

Grandin, R., Jacques, E., Nercessian, A., Ayele, A., Doubre, C., Socquet, A., Kassim, M., Lemarchand, A. & King, G. C. P. (2011). Seismicity during lateral dike propagation: Insights from new data in the recent Manda Hararo–Dabbahu rifting episode (Afar, Ethiopia). *Geochemistry, Geophysics, Geosystems*, **12**(4).

Grimison, N. L., & Chen, W. P., 1988. Earthquakes in the Davie Ridge-Madagascar region and the southern Nubian-Somalian plate boundary. *Journal of Geophysical Research: Solid Earth*, **93**(B9), 10439-10450.

Gudmundsson, A., Lecoeur, N., Mohajeri N. & Thordarson, T., 2014. Dike emplacement at Bardarbunga, Iceland, induces unusual stress changes, caldera deformation, and earthquakes, *Bull. Volcanol.*, **76**:869, doi:10.1007/s00445-014-0869-8.

Hachim S., 2004. Catastrophes : Mayotte perd sa mémoire ! Catastrophes naturelles et mémoire collective à Mayotte. Mémoire de DEA de Géographie. Université Paul Valéry, Montpellier III.

Hanka, W., Saul, J., Weber, B., Becker, J., Harjadi, P., Fauzi, P., Rudloff, A., Bossu R. Ottemöller, L. & Clinton, J., 2010. Real-time earthquake monitoring for tsunami warning in the Indian Ocean and beyond. Natural Hazards & Earth System Sciences, 10(12).

Hartnady, C. J. H., 2002. Earthquake hazard in Africa: perspectives on the Nubia-Somalia boundary: news and view. *South African journal of science*, **98**(9-10), 425-428.

Hendriyana, A., & Tsuji, T., 2019. Migration of very long period seismicity at Aso volcano, Japan, associated with the 2016 Kumamoto earthquake. *Geophysical Research Letters*, **46**. https://doi.org/10.1029/2019GL082645

Horner Johnson, B.C., Gordon, R.G. & Argus, D.F., 2007. Plate kinematic evidence for the existence of a distinct plate between the Nubian and Somalian plates along the Southwest Indian Ridge, *Journal of Geophysical Research: Solid Earth*, **112**(B5).

International Seismological Centre, 2016. On-line Bulletin, http://www.isc.ac.uk, Internatl. Seismol. Cent., Thatcham, United Kingdom, http://doi.org/10.31905/D808B830

Kawakatsu, H., Kaneshima, S., Matsubayashi, H., Ohminato, T., Sudo, Y., Tsutsui, T., Uhira, K., Yamasato, H., Ito, H. & Legrand, D., 2000. Aso94: Aso seismic observation with broadband instruments. *Journal of Volcanology and Geothermal Research*, **101**(1-2), 129-154.

Kennett, B.L.N., 1991. IASPEI, 1991. Seismological tables, Research School of Earth Sciences, Australian National University.

Klimke, J., Franke, D., Gaedicke, C., Schreckenberger, B., Schnabel, M., Stollhofen, H., Rose, J. & Chaheire, M., 2016. How to identify oceanic crust—Evidence for a complex break-up in the Mozambique Channel, off East Africa, *Tectonophysics*, **693**, 436-452.

Klügel, A., Longpré, M.A., García-Cañada, L. & Stix, J., 2015. Deep intrusions, lateral magma transport and related uplift at ocean island volcanoes, *Earth Planet. Sci. Lett.*, **431**, 140-149.

Kumagai, H., & Chouet, B. A., 1999. The complex frequencies of long-period seismic events as probes of fluid composition beneath volcanoes. *Geophysical Journal International*, **138**(2), F7-F12.

Kumagai, H., & Chouet, B. A., 2000. Acoustic properties of a crack containing magmatic or hydrothermal fluids. *Journal of Geophysical Research: Solid Earth*, **105**(B11), 25493-25512.

Kumagai, H., Miyakawa, K., Negishi, H., Inoue, H., Obara, K., & Suetsugu, D., 2003. Magmatic dike resonances inferred from very-long-period seismic signals. *Science*, **299**(5615), 2058-2061.

Kumagai, H. (2006). Temporal evolution of a magmatic dike system inferred from the complex frequencies of very long period seismic signals. *Journal of Geophysical Research: Solid Earth*, **111**(B6).

Lambert, J., 1997. Contribution au relevé de la sismicité historique des îles de la Réunion, de Maurice et des Comores, *BRGM R39736*, 56 p.

López, C., Blanco, M. J., Abella, R., Brenes, B., Cabrera Rodríguez, V. M., Casas, B., Domínguez Cerdeña, I., Felpeto, A., Fernández de Villalta, M., del Fresno, C., García, O., García-Arias, M. J., García-Cañada, L., Gomis Moreno, A., González-Alonso, E., Guzmán Pérez, J., Iribarren, I., López-Díaz, R., Luengo-Oroz, N., Mletlidis, S., Moreno, M., Moure, D., Pereda de Pablo, J., Rodero, C., Romero, E., Sainz-Maza, S., Sentre Domingo, M. A., Torres, P. A., Trigo, P., Villasante-Marcos, V., 2012. Monitoring the volcanic unrest of El Hierro (Canary Islands) before the onset of the 2011–2012 submarine eruption. *Geophysical Research Letters*, **39**(13).

Malod, J.A., Mougenot, D., Raillard, S. & Maillard, A., 1991. Nouvelles contraintes sur la cinématique de Madagascar : les structures de la chaîne de Davie, *C. R. Acad. Sci. Paris*, **312**, Série II, P. 1639-1646.

McNutt, S. R. (2005). Volcanic seismology. *Annu. Rev. Earth Planet. Sci.*, ***32***, 461-491.

Martí, J., Pinel, V., López, C., Geyer, A., Abella, R., Tárraga, M., Blanco, M. J., Castro, A. & Rodríguez, C., 2013. Causes and mechanisms of the 2011–2012 El Hierro (Canary Islands) submarine eruption. *Journal of Geophysical Research: Solid Earth*, **118**(3), 823-839.

Michon, L., 2016. The Volcanism of the Comoros Archipelago Integrated at a Regional Scale. In : Active Volcanoes of the Southwest Indian Ocean, Active Volcanoes of the World. P. Bachelery et al (Eds.).

Mogi, K., 1958. Relations between the eruptions of various volcanoes and the deformations of the ground surfaces around them, *Bull. Earthquake Res. Inst. Univ. Tokyo*, **36**, 99-134.

Nagy, W., 1996. New region-dependent travel-time handling facilities at the IDC; Functionality, testing and implementation details, Tech.Rep. 96/1179, SAIC.

Nehlig P., Lacquement F., Bernard J., Audru J.-C., Caroff M., Deparis J., Jaouen T., Pelletier A.-A., Perrin J., Prognon C., Vittecoq B., 2013. Notice explicative, carte géol. France (1/30 000), feuille Mayotte (1179). Orléans : BRGM, 74 p. Carte géologique par Lacquement F., Nehlig P, Bernard J., 2013.

Nougier, J., Cantagrel, J.M., & Karche, J.P., 1986. The Comores archipelago in the western Indian Ocean: volcanology, geochronology and geodynamic setting, *Journal of African Earth Sciences (1983)*, **5**(2), 135-144.

Okada, Y., 1992. Internal deformation due to shear and tensile faults in a half space, *Bull. Seism. Soc. America*, **82**, 1018–1040.

Papageorgiou, E.; Foumelis, M.; Trasatti, E.; Ventura, G.; Raucoules, D.; Mouratidis, A. Multi-Sensor SAR Geodetic Imaging and Modelling of Santorini Volcano Post-Unrest Response. Remote Sens. 2019, 11, 259.

Pelleter, A.A., Caroff, M., Cordier, C., Bachèlery, P., Nehlig, P., Debeuf, D., & Arnaud, N., 2014. Melilite-bearing lavas in Mayotte (France): An insight into the mantle source below the Comores, *Lithos*, **208**, 281-297.

Piqué, A., 1999. The geological evolution of Madagascar: an introduction. *Journal of African Earth Sciences*, **4**(28), 919-930.

Rabinowitz, P. D., ra, M. F. & Falvey, D., 1983. The separation of Madagascar and Africa. *Science*, **220**(4592), 67-69.

Recq, M. (1982). Anomalies de propagation des ondes Pà l'est de la ride de Davie. *Tectonophysics*, **82**(3-4), 189-206.

RESIF ; (1995). RESIF-RAP French Accelerometric Network ; RESIF - Réseau Sismologique et géodésique Français. doi : 10.15778/RESIF.RA http://dx.doi.org/10.15778/RESIF.RA

REVOSIMA (2019), Bulletin n°1 de l'activité sismo-volcanique à Mayotte, IPGP, Université de Paris, OVPF, BRGM, Ifremer, CNRS, August, 23th, 2019, http://www.ipgp.fr/sites/default/files/ipgp_1er_bulletin_info_sismo_volcanique_mayotte-cor.pdf and www.ipgp.fr/revosimaRindraharisaona, E. J., Guidarelli, M., Aoudia, A., & Rambolamanana, G., 2013. Earth structure and instrumental seismicity of Madagascar: Implications on the seismotectonics. *Tectonophysics*, **594**, 165-181.

Roach, P., J. Milsom, C. Toland, C. Matchette-Downes, C. Budden, D. Riaroh, And N. Houmadi, 2017. Neo evidence supports presence of continental crust beneath the Comoros: Pesgb/Hgs Africa Conference. Aug 2017.

Saria, E., Calais, E., Stamps, D.S., Delvaux, S. & Hartnady, C.J.H., 2014. Present-day kinematics of the East African Rift, *J. Geophys. Res. Solid Earth*, **119**, doi:10.1002/2013JB010901.

Sauter, D., Ringenbach, J. C., Cannat, M., Maurin, T., Manatschal, G., & Mcdermott, K. G., 2018. Intraplate deformation of oceanic crust in the West Somalie Basin: insights from long-offset reflection seismic data, *Tectonics*, **37**, 588–603. https://Doi.Org/10.1002/2017tc004700

Scripps Institution of Oceanography, 1986. IRIS/IDA Seismic Network. International Federation of Digital Seismograph Networks. Other/Seismic Network. doi.org/10.7914/SN/II

Ségoufin, J. & Patriat, P., 1981. Reconstructions of the western Indian Ocean at anomalies M21, M2 and 34 times. Madagascar paleoposition, *Bull. Soc. Géol. France*, **6**, 603-607.

Shapiro, N. M., Droznin, D. V., Droznina, S. Y., Senyukov, S. L., Gusev, A. A., & Gordeev, E. I., 2017. Deep and shallow long-period volcanic seismicity linked by fluid-pressure transfer. *Nature Geoscience*, **10**(6), 442.

SHOM, 2015. MNT Bathymétrique de façade Atlantique (Projet Homonim). http://dx.doi.org/10.17183/MNT_ATL100m_HOMONIM_WGS84

Sigmundsson, F., Hooper, A., Hreinsdóttir, S., Vogfjörd, K. S., Ófeigsson, B. G., Heimisson, E. R., Dumont, S., Parks, M., Spaans, K., Gudmundsson, G. B., Drouin, V., Arnadóttir, T., Jónsdóttir, K., Gudmundsson, M. T., Högnadóttir, T., Fridriksdóttir, Hensch, M., Einarsson, P., Magnússon, E., Samsonov, S., Brandsdóttir, B., White, R., S., Agústsdóttir, T., Greenfield, T., Green, R. G., Hjartardóttir, A., R., Pedersen, R., Bennett, R., A., Geirsson, H., La Femina, P., C., Björnsson, H., Pálsson, F., Sturkell, E., Bean, C., J., Möllhoff, M., Braiden, A. K. & Eibl, E. P.,S., 2015. Segmented lateral dyke growth in a rifting event at Bárðarbunga volcanic system, Iceland. *Nature*, **517**(7533), 191.

SISFRANCE-Océan Indien, 2010. BRGM http://www.sisfrance.net/Reunion/index.asp

Stamps, D. S., Saria, E. & Kreemer, C., 2018. Geodetic Strain Rate Model for the East African Rift System, *Scientific reports*, **8**(1), 732.

Talandier, J., Hyvernaud, O., & Maury, R. C., 2016. Unusual seismic activity in 2011 and 2013 at the submarine volcano Rocard, society hot spot (French Polynesia). *Geophys. Res. Lett*., **43**, 4247-4254, doi: 10.1002/2016GL068342.

Talwani, M., 1962. Gravity measurements on HMS Acheron in south Atlantic and Indian Oceans. *Geological Society of America Bulletin*, **73**(9), 1171-1182.

Thordarson, T., & Self, S. (1993). The Laki (Skaftár Fires) and Grímsvötn eruptions in 1783–1785. Bulletin of Volcanology, 55(4), 233-263.

Toda, S., Stein, R.S. & Sagiya, T., 2002. Evidence from the AD 2000 Izu islands earthquake swarm that stressing rate governs seismicity, *Nature*, **419**(6902), 58.

Vienne E., 1900. Notice sur Mayotte et les Comores. Impr Alcan-Lévy, Paris 200p. ark:/12148/bpt6k57903288

Weatherall, P., Marks, K. M., Jakobsson, M., Schmitt, T., Tani, S., Arndt, J. E., Rovere, M., Chayes, D., Ferrini, V. & Wigley, R. (2015). A new digital bathymetric model of the world's oceans. *Earth and Space Science*, **2**(8), 331-345.

Wegmüller, U.;Werner, C.; Strozzi, T.;Wiesmann, A.; Frey, O.; Santoro, M. Sentinel-1 Support in the GAMMA Software. Procedia Comput. Sci. 2016, 100, 1305–1312.

Weichert, D.H., 1980. Estimation of the earthquake recurrence parameters for unequal observation periods for different magnitudes, *Bulletin of the Seismological Society of America*, **70**(4), 1337-1346.

Wessel, P. & Smith,W.H.F., 1995. New version of the generic mapping tools released, *EOS, Trans. Am. geophys. Un.*, **76,** 329.

White, R., & McCausland, W. (2016). Volcano-tectonic earthquakes: A new tool for estimating intrusive volumes and forecasting eruptions. *Journal of Volcanology and Geothermal Research*, **309**, 139-155.

Wyss M, Shimazaki S & Wiemer S., 1997. Mapping active magma chambers beneath the off-Ito volcano, Japan, *Journal of Geophysical Research: Solid Earth*, **102**:413–20.

Zinke, J., Reijmer, J.J.G., Thomassin, B.A., Dullo, W.C., Grootes, P.M. & Erlenkeuser, H., 2003a. Postglacial flooding history of Mayotte lagoon (Comoro archipelago, southwest Indian Ocean), *Marine Geology*, **194**(3-4), 181-196.

Zinke, J., Reijmer, J.J.G. & Thomassin, B.A., 2003b. Systems tracts sedimentology in the lagoon of Mayotte associated with the Holocene transgression, *Sedimentary Geology*, **160**(1-3), 57-79.

Date	Start	End	Observations
02/09/2018	08:38	8:55	Several small high frequency events and different successive lobes of monochromatic low frequency waves. Peak at 0.062 Hz in the fast Fourier transform (FFT).
02/09/2018	11:12	11:32	Many repeating high frequency events associated with a long sequence of monochromatic low frequency waves.
11/11/2018	09:27	09:47	Several small repeating high frequency events within the sequence of monochromatic low frequency waves. Peak at 0.062 Hz in the FFT. Waveform very similar to event 2.

Table 1. The three largest tremors recorded between May and November 2018. Timings are reported from local MCHI or YTMZ stations.

Site	Name	Owner	Long	Lat
GAMO	M’Tangamouji	EXAGONE (TERIA)	45.0848	-12.7615

MTSA	M’Tangamouji	Precision Topo (Lél@sarl)	45.0789	-12.7616
KAWE	Kawéni	Precision Topo (Lél@sarl)	45.2251	-12.7670
MAYG	Dzaoudzi	CNES	45.2582	-12.7821
PORO	Poroani	Precision Topo (Lél@sarl)	45.1440	-12.8975
BDRL	Bandrélé	EXAGONE (TERIA)	45.1928	-12.9109

Table 2. The GNSS stations with name, owner, and coordinates (location map in Fig. 12)

	Phase D velocity (mm/yr)			Phase D model (mm/yr)			Residuals (mm/yr)		
Site	East	North	Up	East	North	Up	East	North	Up
GAMO	172	-4	-69	153	-5	-78	19	1	9
MTSA	173	-5	-83	151	-5	-76	22	0	7
KAWE	202	-12	-139	227	-6	-160	25	6	21
MAYG	176	2	-133	248	4	-192	72	2	59
PORO	180	51	-114	166	46	-96	14	5	18
BDRL	184	77	-125	184	63	-119	0	14	6

Table 3. Velocity anomalies at the Mayotte GNSS stations during deformation phase D from July 3rd to November 14th, 2018, assuming a linear trend (observations, model, and residuals).

			BDRL	**GAMO**	**KAWE**	**MAYG**
			mm yr^{-1}	mm yr^{-1}	mm yr^{-1}	mm yr^{-1}
East	D1	11/7/18-11/10/18	175	163	173	168
	D2	11/10/18-11/1/19	235	220	251	224
	D3	11/1/19-11/4/19	227	194	213	203
	D4	11/4/19-11/7/19	121	107	112	103
North	D1	11/7/18-11/10/18	74	-1	-12	4
	D2	11/10/18-11/1/19	99	-19	-29	-9
	D3	11/1/19-11/4/19	71	-16	-19	-19
	D4	11/4/19-11/7/19	51	-16	-13	-3
Vertical	D1	11/7/18-11/10/18	-113	-57	-120	-115
	D2	11/10/18-11/1/19	-171	-126	-185	-186
	D3	11/1/19-11/4/19	-159	-67	-152	-161
	D4	11/4/19-11/7/19	-82	-62	-87	-103

Table 4. Temporal evolution of the velocity anomalies at stations BDRL, GAMO, KAWE, and MAYG.

	Observed Total phase C			C_reservoir (*)			C_conduit (observation)			C_conduit (model)			Residuals		
Site	East	North	Up	East	North	Up	East	North	Up	East	North	Up	East	North	Up
	mm	mm	mm	mm	mm	mm	mm	mm	mm	mm	mm	mm	mm	mm	mm
GAMO	0	-4	-9	11	0	-4	-11	-4	-5	-8	-2	1	-3	-2	-6

MTSA	1	-4	5	11	0	-5	-10	-4	10	-8	-2	1	-2	-2	9
KAWE	0	-3	-8	13	-1	-9	-13	-2	1	-13	-3	3	0	1	-2
MAYG	0	-6	-9	11	0	-8	-11	-6	-1	-17	-4	4	6	-2	-5
PORO	0	-2	0	11	3	-7	-11	-5	7	-13	-6	2	2	1	5
BDRL	-6	-7	-10	12	5	-8	-18	-15	-2	-16	-8	2	-2	-7	-4

Table. 4. Deformation in phase C split into two contributions: deflation of the reservoir & inflation of the feeding conduit. The values in the column C_reservoir (*) are estimated by scaling the rates of phase D by 55% for 42 days (from Tab. 3). The modelling of the conduit parameters assumes that the centre of the conduit is above the centre of the reservoir.

	Phase B			Model			Residuals		
Site	East	North	Up	East	North	Up	East	North	Up
	mm	mm	mm	mm	mm	mm	mm	mm	mm
GAMO	5	-2	0	3	-1	0	2	-1	0
MTSA	5	0	0	3	-1	0	2	1	0
KAWE	6	-3	0	6	-1	0	0	-2	0
MAYG	3	-1	-1	6	-2	0	-3	1	-1
PORO	2	-2	0	1	-1	0	1	-1	0
BDRL	4	-1	0	1	-1	0	3	0	0

Table 5. Deformation during phase B from May 15th to May 30th. We assume that the fault has the same geometry as the conduct of phase C: a rectangular fault of 20 km height, 4 km extension, and slip 0.85 m.

Phase	**Mean date**	**Effusion rate**		**rms fit**
		km^3 yr^{-1}	m^3 s^{-1}	cm
D1	20/08/2018	2.30	72.9	1.60
D2	20/11/2018	2.96	93.8	2.68
D3	20/02/2019	2.43	77.0	2.25
D4	20/05/2019	1.40	44.4	1.43

Table 6. Evolution of the effusion rate estimated over periods of three months each

Phase	**Mean date**	**Main reservoir**		**Secondary reservoir**		**rms fit**
		km^3 yr^{-1}	m^3 s^{-1}	km^3 yr^{-1}	m^3 s^{-1}	cm
D1	20/08/2018	2.30	72.9	0.00	0.0	1.59
D2	20/11/2018	2.92	92.5	0.12	3.8	2.06
D3	20/02/2019	2.43	77.0	0.11	3.5	2.05
D4	20/05/2019	1.28	40.6	0.08	2.5	1.09

Table 7. Evolution of the effusion rate estimated over periods of three months each by assuming a dual source

Depth	UTM	UTM	Long.	Single source		Dual source		
	East	North		effusive rate	rms fit	effusive rate (main)	effusive rate (secondary)	rms fit
km	km	Km	°	km^3 y^{r-1}	mm	km^3 y^{r-1}	km^3 y^{r-1}	Mm
24	561	8587	45.56	2.56	29.67	2.34	0.11	22.17
28	567	8587	45.62	3.5	26.09	3.17	0.13	19.34
32	571	8587	45.65	4.18	23.24	3.94	0.14	18.04
36	578	8587	45.72	5.39	21.67	5.09	0.17	16.16
40	585	8587	45.78	6.66	20.68	6.42	0.19	14.67

Table 8. Analysis of the fits and effusive volumes as a function of source depth and model type (single v/s dual) in the case of phase D2 (period from October 5th, 2018 to January 5th, 2019)

Site	Long	Lat	Distance (km)	vE (mm yr^{-1})	vN (mm yr^{-1})
Grande Ile Glorieuse	47.30	-11.58	215	-15	-12
Mutsamudu (Anjouan)	44.39	-12.17	160	29	-14
Moroni (Grande Comore)	43.25	-11.71	260	9	-4

Table 6. Predicted horizontal velocity anomalies at three nearby islands, assuming the deflation rate of 82 m^3 s^{-1} for phase D.

APPENDICES

Site		Long	Lat	v_E	v_N	σ_E	σ_N	r_E	r_N
		°	°	mm/yr	mm/yr	mm/yr	mm/yr	mm/yr	mm/yr
ABPO	Madagascar	47.229	-19.018	18.5	14.0	0.2	0.2	-1.2	-0.1
ARSH	Tanzania	36.698	-3.387	24.5	17.5	0.3	0.3	-0.8	-0.4
ASOS	Ethiopia	34.553	10.051	22.9	17.9	0.2	0.2	-7.3	-0.8
DODM	Tanzania	35.748	-6.186	22.2	18.0	0.3	0.3	-2.1	-0.3
EBBE	Uganda	32.445	0.038	24.9	16.3	0.2	0.2	-1.7	-3.1
ERAS	South Africa	27.696	-23.687	18.2	18.2	0.2	0.2	0.2	-3.0
FG04	Uganda	32.587	0.313	24.0	16.5	0.4	0.3	-2.7	-2.9
GETA	Tanzania	32.217	-2.881	24.6	18.7	0.4	0.4	-0.9	-0.8
INHB	Mozambique	35.383	-23.871	18.5	17.9	0.4	0.4	0.5	-0.5
KASM	Zambia	31.225	-10.172	20.5	18.1	0.2	0.2	-2.4	-1.8
LLNG	Malawi	33.789	-13.947	19.6	17.4	0.3	0.3	-1.9	-1.6
MAL2	Kenya	40.194	-2.996	26.5	15.8	0.2	0.2	1.0	-0.9
MAYG	Mayotte	45.258	-12.782	21.9	14.8	0.2	0.2	0.0	0.0
METU	Ethiopia	35.586	8.271	23.2	17.8	0.3	0.3	-6.3	-0.5
MOIU	Kenya	35.290	0.288	24.4	18.3	0.2	0.2	-2.3	-0.1
MPIK	Zambia	31.451	-11.821	20.4	18.1	0.3	0.3	-1.9	-1.7
MTVE	Tanzania	40.166	-10.260	23.2	15.7	0.2	0.2	0.3	-1.0
NEGE	Ethiopia	39.589	5.335	28.0	17.3	0.2	0.2	-0.5	0.4
NMPL	Mozambique	39.258	-15.123	20.0	16.2	0.4	0.4	-1.1	-0.8
PANO	Réunion	55.687	-21.002	16.2	12.8	0.3	0.3	-2.8	1.7
PBWA	South Africa	31.134	-23.952	17.8	17.8	0.2	0.2	-0.1	-2.1
PMBA	Mozambique	40.484	-12.964	20.5	15.9	0.4	0.4	-1.4	-0.7
RCMN	Kenya	36.893	-1.221	26.4	17.0	0.2	0.2	0.3	-0.8
RDRG	Rodrigues	63.426	-19.681	17.2	8.8	0.3	0.3	-2.3	0.5
SEYG	Seychelles	55.531	-4.679	25.6	12.0	0.2	0.2	0.7	0.9
SLEU	Réunion	55.572	-21.208	16.4	12.4	0.2	0.2	-2.5	1.3
TANZ	Tanzania	39.208	-6.766	22.2	17.0	0.2	0.2	-1.9	0.0
TDOU	South Africa	30.384	-23.080	17.9	17.7	0.2	0.2	-0.3	-2.5
TETE	Mozambique	33.576	-16.147	19.0	17.7	0.3	0.3	-1.7	-1.3
TEZI	Zambia	26.016	-15.747	19.4	18.8	0.2	0.2	-1.5	-3.0
TNDC	Tanzania	37.341	-11.063	22.2	16.9	0.2	0.2	-0.4	-0.8

ULUB	DRC	27.485	-11.631	23.3	19.5	0.3	0.3	0.9	-1.7
VACS	Mauricius	57.497	-20.297	17.0	11.0	0.2	0.2	-2.2	0.6
VHMR	Madagascar	49.921	-13.458	21.6	14.6	0.5	0.5	-0.1	1.4
VOIM	Madagascar	46.793	-21.906	18.2	14.4	0.3	0.3	-0.5	0.1
ZAMB	Zambia	28.311	-15.426	20.3	18.2	0.2	0.2	-0.7	-2.7
ZBMT	Madagascar	44.733	-22.827	17.0	15.2	0.5	0.5	-1.3	0.2

Appendix 1. ITRF2014 horizontal velocity of GNSS stations around Mayotte. The time series are from the Nevada geodetic laboratory (Blewitt et al., 2018). The two right columns contain the relative velocities after cancelling the global rotation by applying a clockwise rotation equivalent to 2.1° Myr^{-1} and setting zero motion in MAYG.

Code	Lat	Long	Type of sensor (network)	Location	Implementation
YTMZ	-12.7557	45.2307	Accelerometer (RAP)	Mamoudzou (Mayotte)	continuous
ABPO	-19.0183	47.2292	BB (IRIS/IDA)	Ambohipanompo (Madagascar)	continuous
VOI	-21.9065	46.7933	BB (GEOFON)	Vohitsoka (Madagascar)	continuous
KIBK	-2.3591	38.0433	BB (GEOFON)	Kibwezi (Kenya)	continuous
SBC	-11.6491	43.2969	BB (Karthala observatory)	Grande Comore	05/30^{-}
CAB	-11.7486	43.3435	BB (Karthala observatory)	Grande Comore	05/30^{-}
MOIN	-11.7659	43.2435	BB (Karthala observatory)	Grande Comore	05/30-08/6
MCHI	-12.8329	45.1237	BB (Edusismo)	Chiconi (Mayotte)	06/27^{-}
RCBF0	-12.7984	45.2748	Raspberry shake 3D	Pamandzi (Mayotte)	06/26-07/10
RAE55	-12.7335	45.2036	Raspberry shake 1D	Koungou (Mayotte)	06/26^{-}
SBV	-13.4584	49.9212	BB (GEOFON)	Sambava (Madacascar)	07/15^{-}

Appendix 2. The eleven stations of the Mayotte virtual seismic network. BB means broadband.

Date	Location			Magnitude		Moment	Plane 1			Plane 2		
	Long	Lat	depth	m_l	M_w	x 10^{16}	Strike	Dip	Rake	Strike	Dip	Rake
	°E	°S	km			N m	°	°	°	°	°	°
14/05/18 14:41	45.83	12.51	36	5.2	5.2	7.2	354	62	4.0	262	87	152
15/05/18 15:48	45.71	12.72	34	5.8	5.9	82.8	347	61	-8	81	83	-151

20/05/18 08:01	45.69	12.72	36	5.0	5.4	17.6	346	47	-4	79	87	-137
21/05/18 00:47	45.70	12.70	38	5.1	5.5	23.4	351	53	-1	82	89	-143
22/05/18 12:37	45.71	12.71	41	5.0	5.0	4.7	330	41	16	227	79	130
25/05/18 05:43	45.68	12.74		5.1								
25/05/18 06:36	45.69	12.73	31	5.4	5.1	6.2	350	73	8	258	82	162
26/05/18 00:32	45.70	12.72	39	5.3	4.9	2.9	341	68	11	247	80	158
28/05/18 22:12	45.76	12.68		5.1								
30/05/18 05:54	45.72	12.72	32	5.6	5.1	5.2	354	69	3	263	87	159
30/05/18 16:21	45.72	12.73		5.1								
01/06/18 03:24	45.72	12.72		5.3								
01/06/18 03:35	45.72	12.74		5.3								
01/06/18 05:44	45.72	12.74		5.2								
01/06/18 07:14	45.70	12.74	42	5.0	5.0	3.4	355	76	7	263	83	166
01/06/18 08:28	45.72	12.74		5.0								
02/06/18 07:42	45.72	12.74		5.2								
02/06/18 17:39	45.72	12.71		5.1								
03/06/18 06:13	45.72	12.74	30	5.2	5.1	6.4	350	68	-9	83	81	-158
04/06/18 18:51	45.73	12.69		5.1								
04/06/18 19:53	45.71	12.75	31	5.4	5.0	4.6	352	73	7.0	260	83	163
04/06/18 21:20	45.73	12.76	22	5.4	5.0	4.5	1	68	-2	92	89	-158
05/06/18 23:02	45.71	12.77	25	5.0	5.1	4.8	347	58	1	257	89	148
06/06/18 09:37	45.72	12.76	22	5.0	4.9	3.3	345	67	11	250	80	156
08/06/18 12:03	45.71	12.71	15	5.0	4.9	3.0	247	62	153	350	67	31
12/06/18 17:17	45.75	12.77	12	5.4	5.4	15.7	4	58	8	269	83	148
23/06/18 19:45	45.73	12.72	12	5.0	5.0	4.2	360	60	7	267	84	149
25/06/18 17:41	45.80	12.73	12	5.0	5.3	10.8	1	57	9	266	82	147
27/06/18 06:40	45.82	12.67	19	5.0	5.2	8.7	1	70	14	267	77	159
28/03/19 01:40	45,53	12,74		5.0								
05/04/19 10:28	45.55	12.66		5.2								
14/05/19 00:20	45.55	12.70		5.1								

Appendix 3. The 32 events with ml ≥ 5.0, 29 occurring during the first 50 days of the crisis between May 15th and June 27th, 2018. For 19 of them, there is an available G-CMT, with fault planes 1 and 2 reported. The G-CMT catalogue listed eight other events with ml between 4.7 and 4.9 occurring in May and June 2018).